2011

Synthesis and binding studies of peptide mimetics, anion receptors, and kinase inhibitors

Nanditha G. Nair

Department: Chemistry

Recommended Citation

Nair, Nanditha G., "Synthesis and binding studies of peptide mimetics, anion receptors, and kinase inhibitors" (2011). *Doctoral Dissertations*. 2093.
https://scholarsmine.mst.edu/doctoral_dissertations/2093

hippocampus are an example of quiescent cells. Such terminally differentiated cells are generally incapable of reentering in to the cell cycle. They will continue their function in G0 phase. Under physiological conditions neurons are subjected to a variety of stimuli and signals. They include mitogenic signals that promote reentry in to the cell cycle and antimitogenic factors which strive to maintain the neurons in the G0 phase. However, conditions such as brain injuries can alter the balance, leading to cell cycle entry. It has been shown that cell cycle proteins are over expressed in AD patients with mild cognitive impairments. These are over expressed even before the appearance of Aβ plaques indicating that cell cycle reentry happens at the early stage of disease.

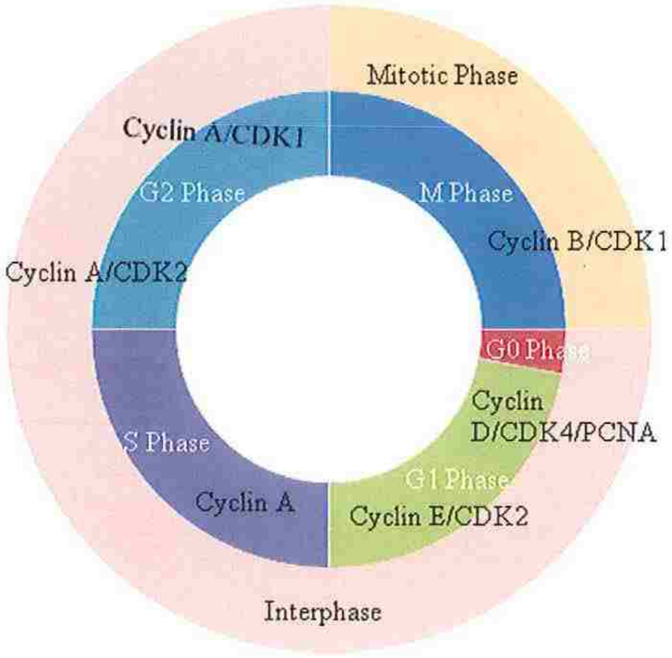

Figure 1.1 Cell cycle proteins and CDKs which are involved in the different phases of the cell cycle.

cycle reentry happens at early stages of AD. The formation of Aβ plaques occurs in the later stage. When neurons, *in vitro* are subjected to Aβ oligomers, but not monomers, there is increase in DNA synthesis, giving further evidence for the importance of Aβ oligomers on cell cycle reentry. The neuronal cells that reenter the cycle undergo apoptosis before reaching the Mitotic stage. Evidences show that Aβ induced neurons proceed to the S phase and replicate DNA. Thus the neurons entering the cell cycle are trapped in or before the s phase. They neither finish dividing nor enter in to the G0 phase.

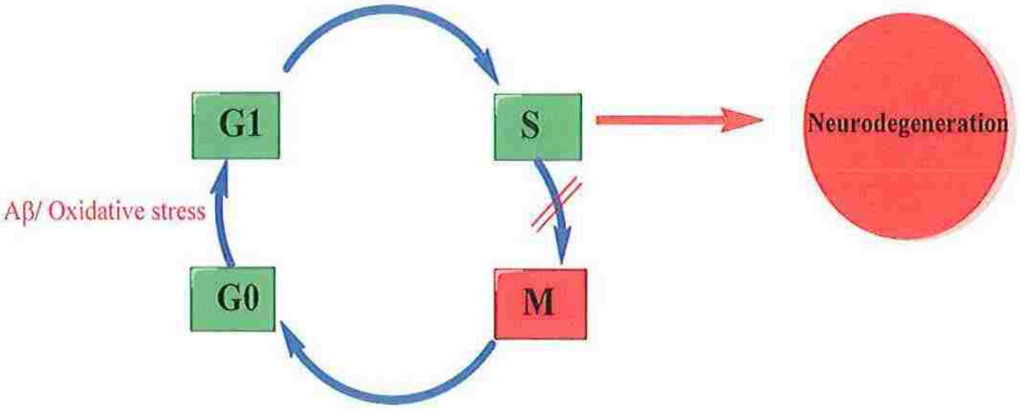

Figure 1.2. Aβ induced neurons proceed to S phase and replicate DNA.

1.1.4 Aβ and CDK5. Aβ plaques occur around the neuron, when the balance of Aβ generation and clearance is altered. Aberrant activation of kinases and inhibition of phosphatases results in elevates the levels of Aβ and Neurofibrillary tangles.

Overactivation of CDK5, mediated by A β results in tau-hyperphosphorylation, decreased

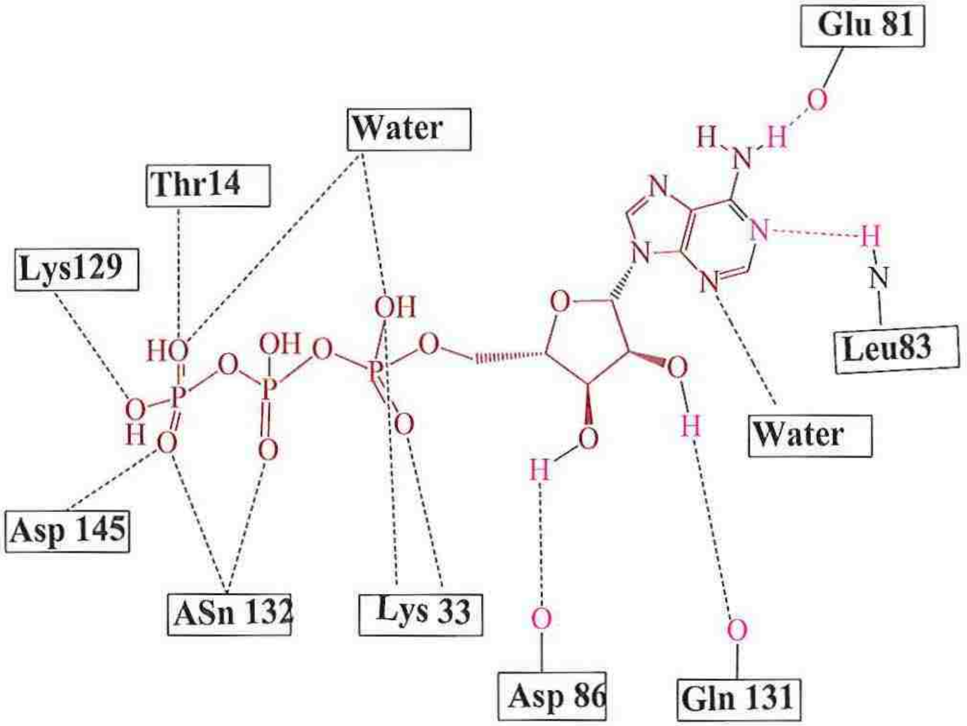

CDK2/ATP

Figure 1.9. Major binding amino acid residues in CDK2 /ATP complex.

ATP competitive inhibitors typically form 1 to 3 hydrogen bonds with the kinase hinge residues. The binding region of inhibitors can be divided in to adenine region, ribose region, phosphate region and hydrophobic region. The adenine region can be occupied by all the inhibitors although with different orientations than ATP. The ability of inhibitors to extend in to hydrophobic region and other region is the key factor in the specificity. The co-crystal structures of roscovitine (2), olomoucine (3), aloisine, inirubin-3'-oxime (8) etc with CDK2 and CDK5/p25 have been reported (Figure 1.10 and Figure 1.11).[66, 105]

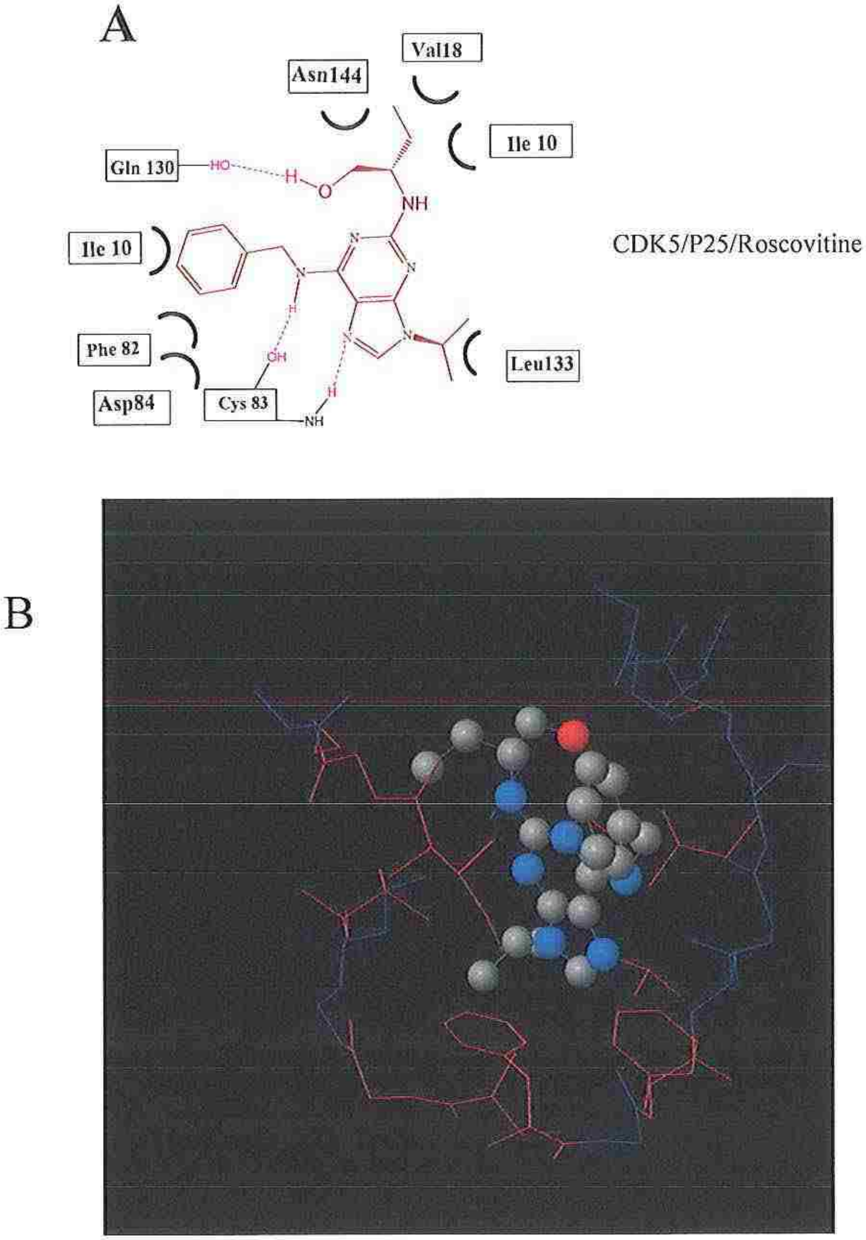

Figure 1.10. Schematic diagram of major aminoacids involved in binding of roscovitine (2) to CDK5/p25 (A). Crystal structure of CDK5/p25-roscovitine showing ligand binding pocket. Hydrophobic region is indicated in red (B)[66] (PDB, DOI:10.2210/pdb1unh/pdb).

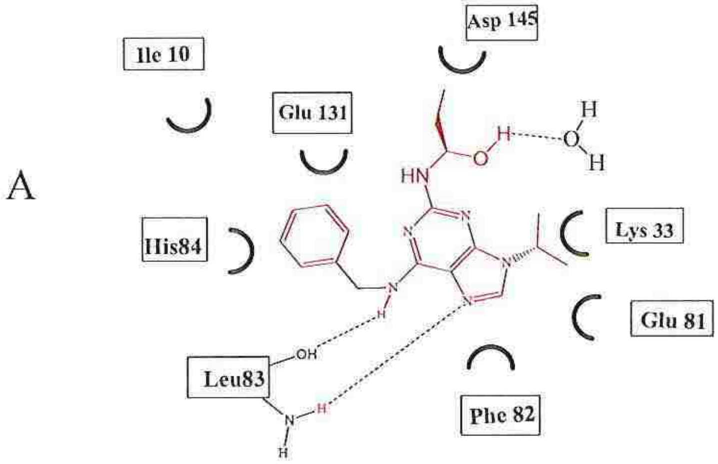

CDK2/Roscovitine

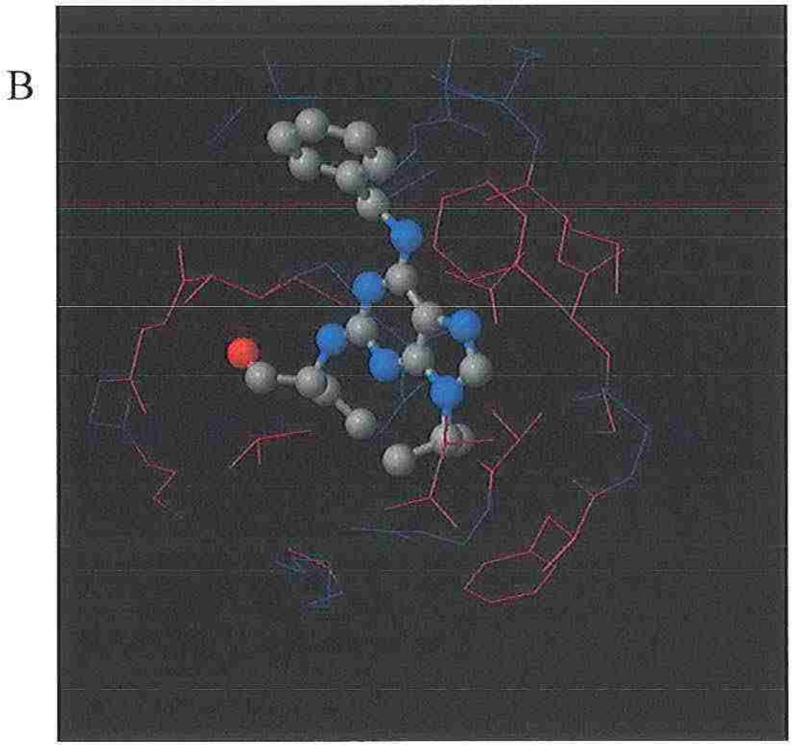

Figure 1.11. Schematic diagram of major aminoacids involved in binding of roscovitine (2) to CDK2 (A).Crystal structure of CDK2.roscovitine (2) showing ligand pocket. Hydrophobic region is indicated in red (B).[106] (PDB, DOI:10.2210/pdb2a4l/pdb).

The intensities of the fluorescence were conveniently analyzed using Scion images. The intensity of the PI fluorescence reflects the relative number of the dead cells as PI cannot permeate the live cell membranes. As shown in Figure 1.15, there is visible difference in the control (in the absence of Aβ oligomers) and the Aβ oligomers-treated cell cultures. Typically 48 h is required for the expression of the Aβ toxicity. These experiments were repeated using the established cell cycle inhibitors, roscovitine (2), flavopiridol (1), and the fluoroaryl substitued purine derived triazoles, compounds 22-24.

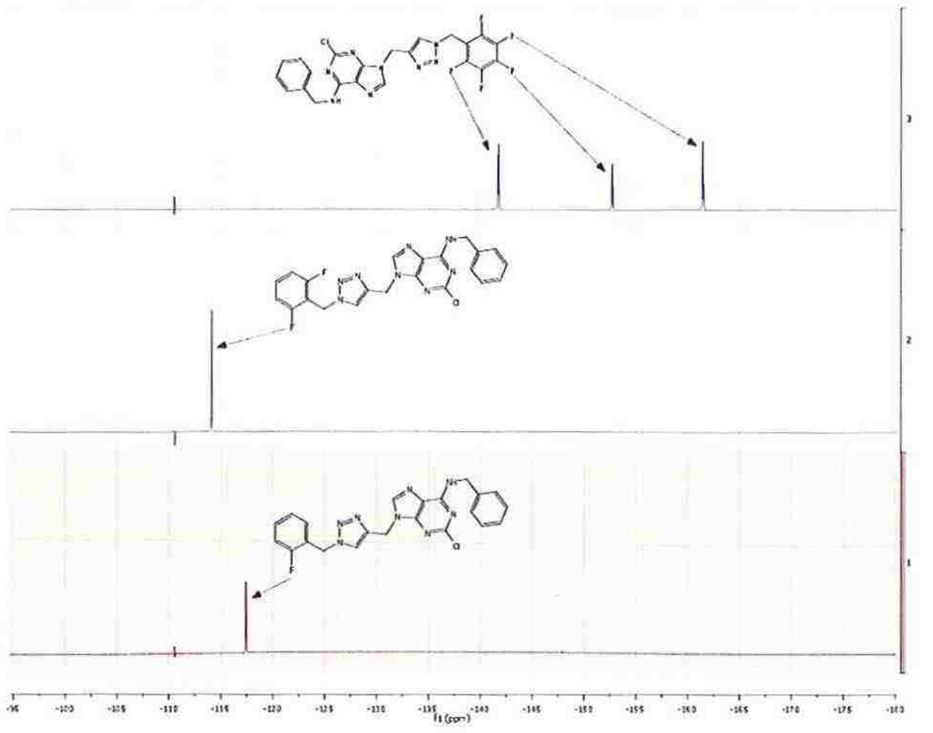

Figure 1.14. ^{19}F spectra of compounds 22, 23 and 24.

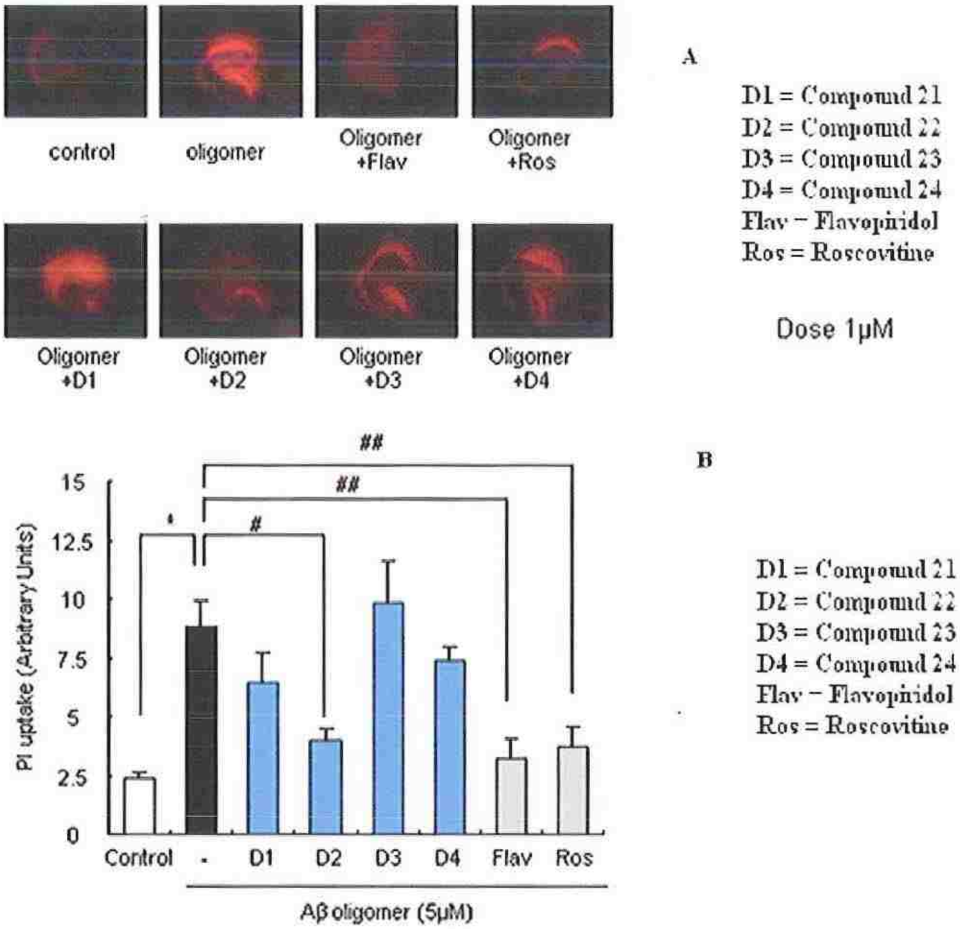

Figure 1.16. Hippocampal slices were incubated with compounds 21.24, or cell cycle inhibitors flavopiridol (1), roscovitine (2) (1 μM) for 1 h and then treated with 5 μM Aβ oligomers in the presence of PI for 48 h. PI uptake was analyzed with microscopy (panel A) to determine the effects of these pharmacological agents on Aβ oligomers-induced toxicity. The relative fluorescence intensities are expressed as arbitrary units of PI uptake (panel B).

1.2.13 Statistical Analysis. Data were expressed as the means ± S.E. of the values from the number of experiments indicated in the corresponding figures. Differences between groups were examined for statistical significance using one-way analysis of variance with an unpaired Students t-test. A *p* value less than 0.05 denoted statistical significance.

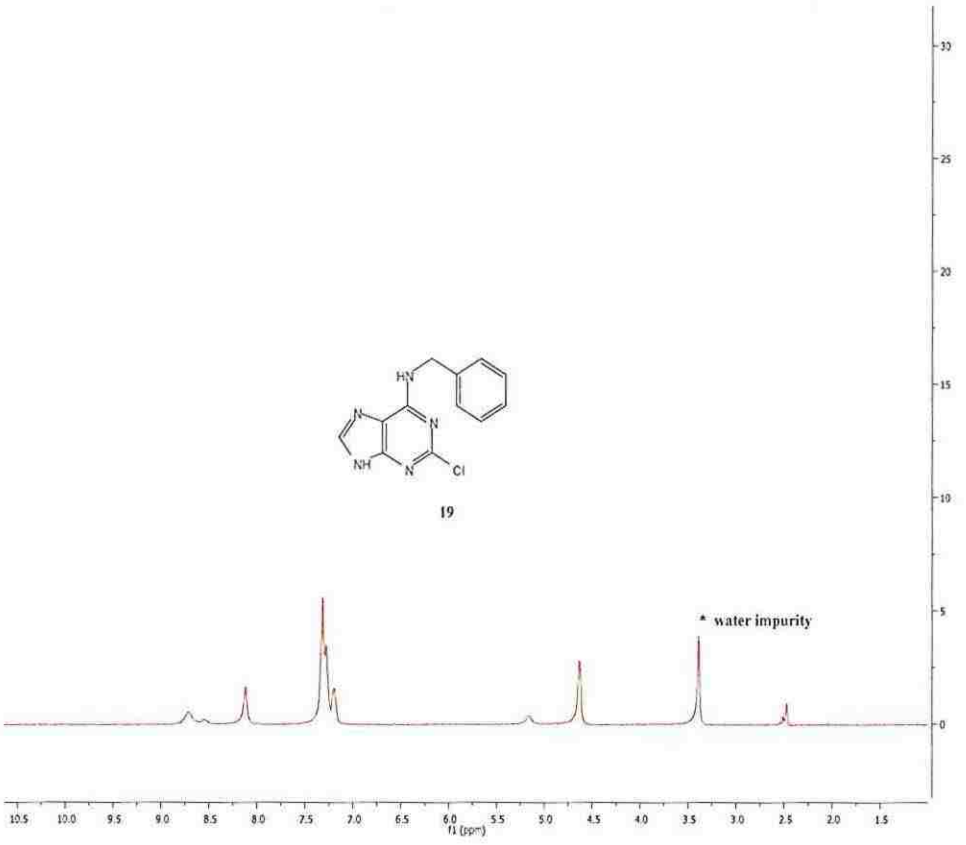

Figure 1.18. ^1H NMR (400MHz) spectra of 2-Chloro-6-benzylaminopurine (19)

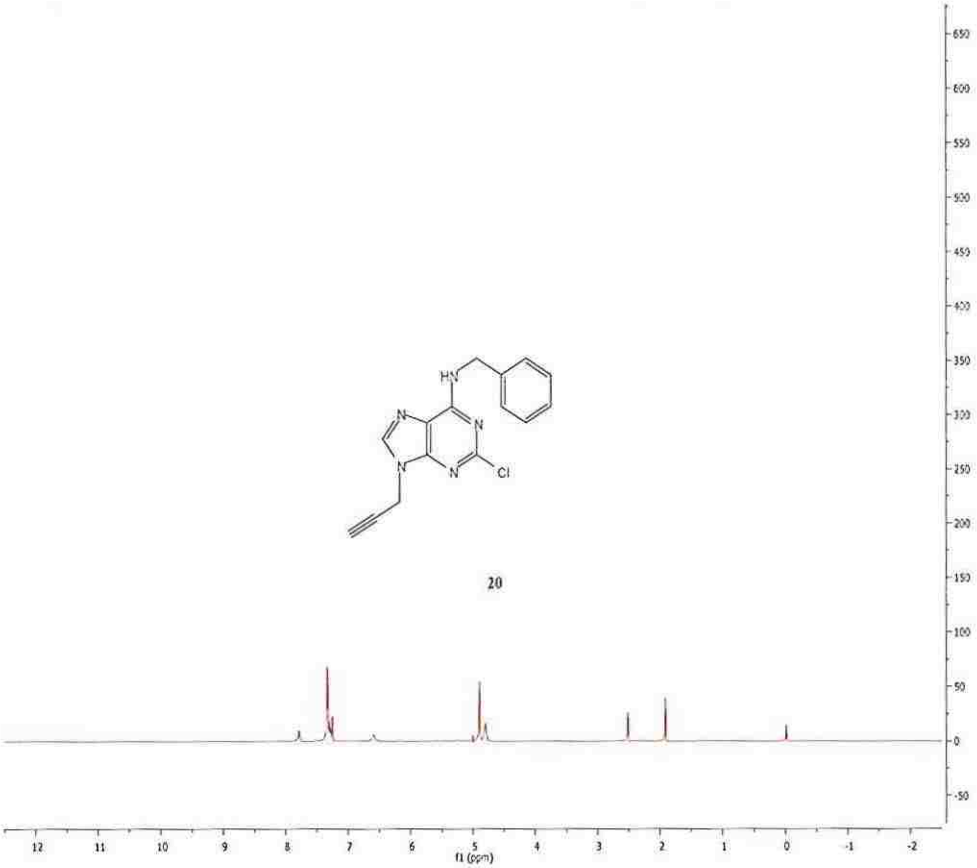

Figure 1.19. ^{1}H NMR (400MHz) spectra of 2.Chloro-6-benzylamino-9-(2-propynyl)purine (20)

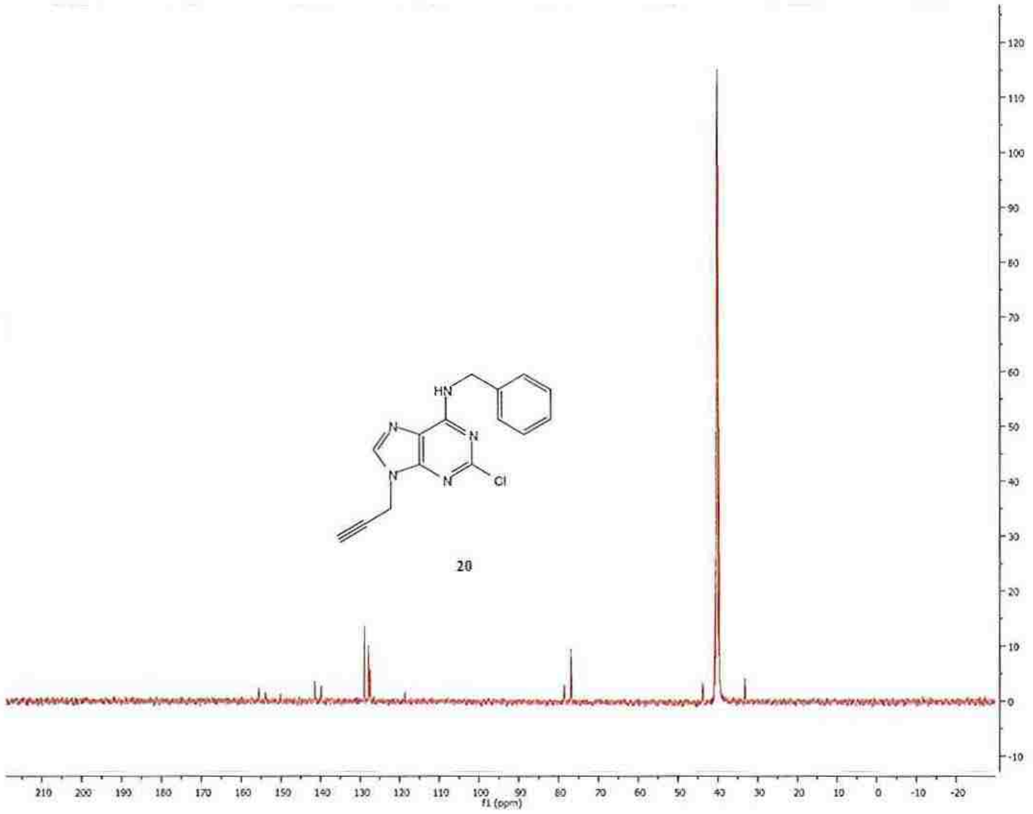

Figure 1.20. ^{13}C NMR (100MHz) spectra of 2-Chloro-6-benzylamino-9-(2-propynyl)purine (20)

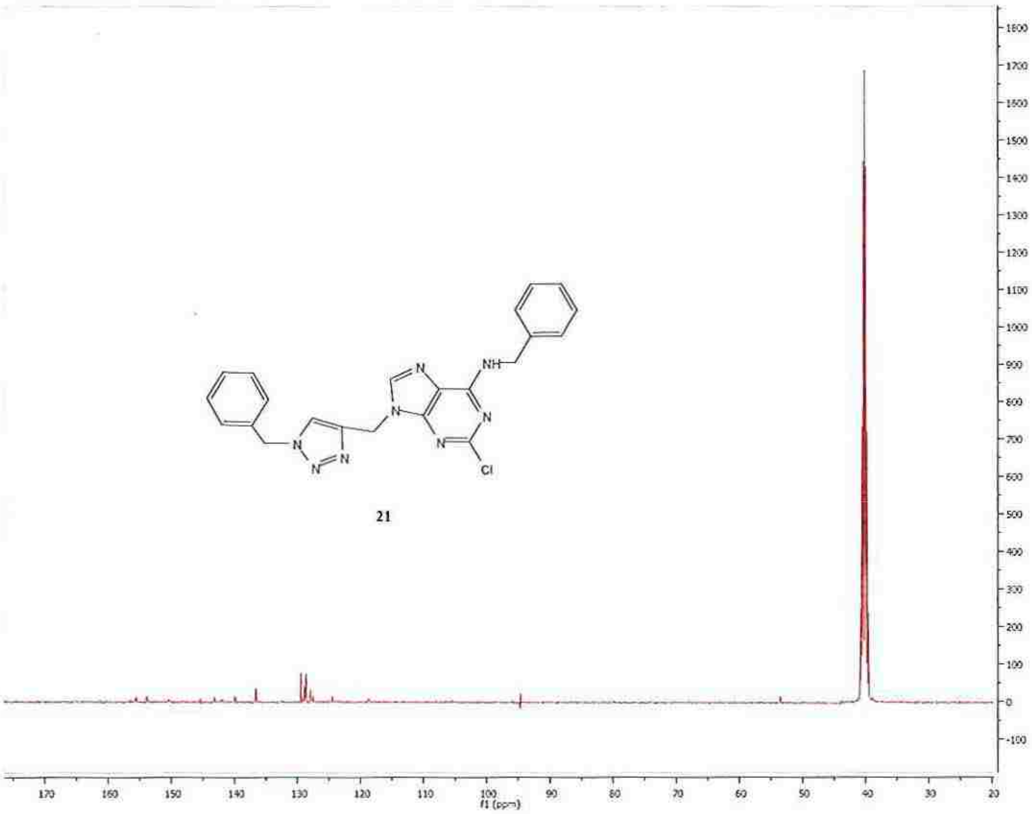

Figure 1.21. ^{13}C NMR (100MHz) spectra of 2-Chloro-6-benzylamino-9-(1-benzyl-1H-1,2,3.triazol-4.yl-methyl)purine (21).

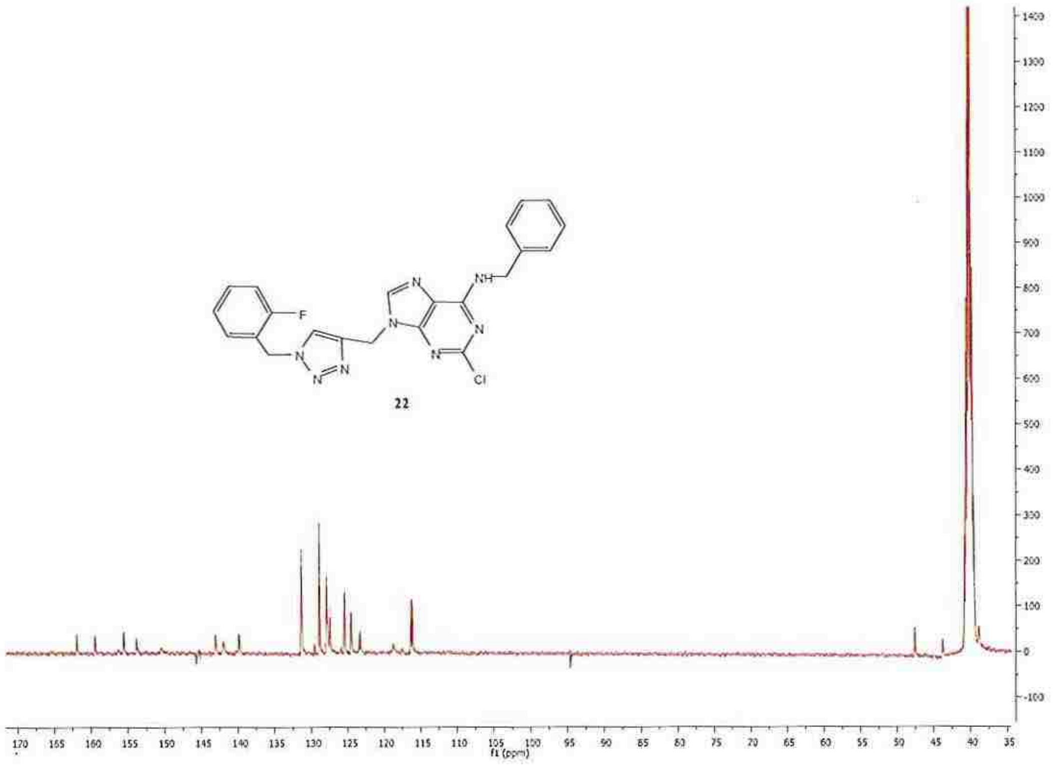

Figure 1.22. ^{13}C NMR (100MHz) spectra of 2-Chloro-6-benzylamino-9-[1-(2-fluorobenzyl)-1H-1,2,3.triazol-4.yl-methyl]purine (22).

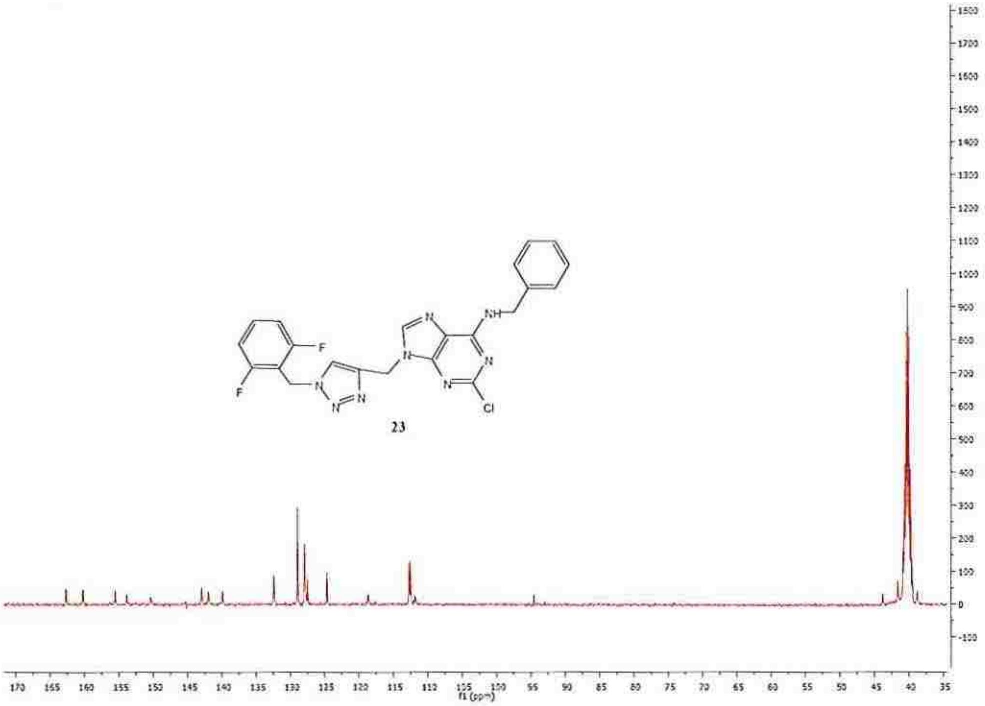

Figure 1.23. ^{13}C NMR (100MHz) spectra of 2.Chloro-6-benzylamino-9-[1-(2,6-difluorobenzyl)-1H-1,2,3.triazol-4-yl-methyl]purine (23).

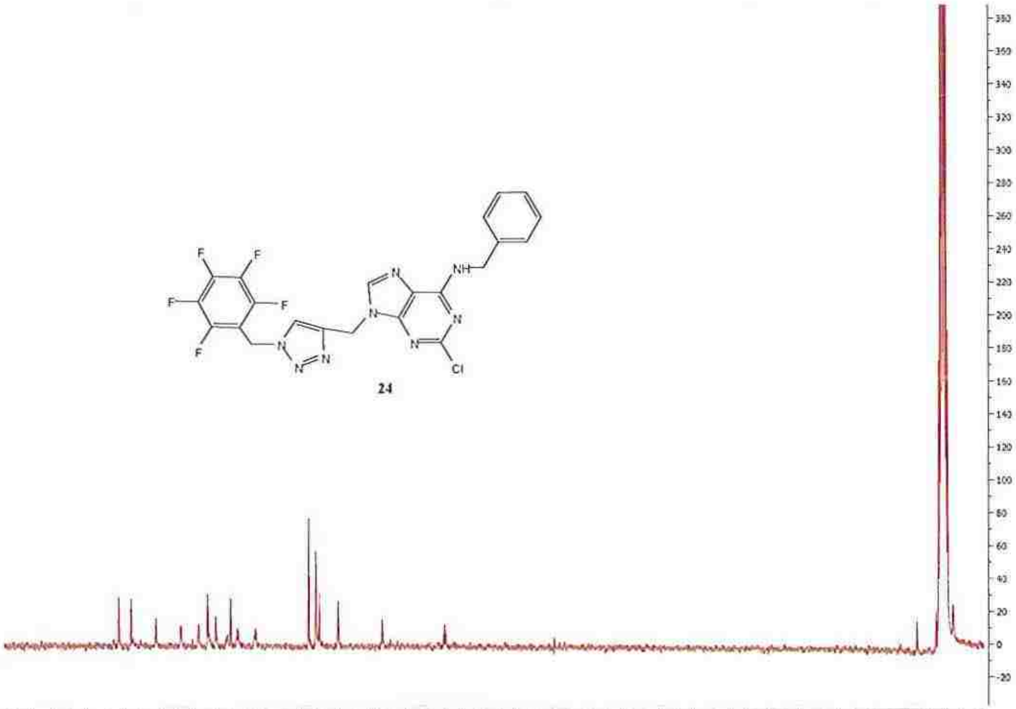

Figure 1.24. ^{13}C NMR (100MHz) spectra of 2.Chloro-6-benzylamino-9-[1-(pentafluorobenzyl)-1H-1,2,3-triazol-4-yl-methyl]purine (24)

[28] Y. Tong, Y. Xu, K. Scearce-Levie, L. J. Ptacek, Y.-H. Fu, COL25A1 triggers and promotes Alzheimer's disease-like pathology in vivo, *Neurogenetics* **2010**, *11*, 41.

[29] A. Alvarez, R. Toro, A. Caceres, R. B. Maccioni, Inhibition of tau phosphorylating protein kinase cdk5 prevents beta-amyloid-induced neuronal death, *FEBS Lett* **1999**, *459*, 421.

[30] J. Ryder, Y. Su, F. Liu, B. Li, Y. Zhou, B. Ni, Divergent roles of GSK3 and CDK5 in APP processing, *Biochem. Biophys. Res. Commun.* **2003**, *312*, 922.

[31] A. McShea, P. L. Harris, K. R. Webster, A. F. Wahl, M. A. Smith, Abnormal expression of the cell cycle regulators P16 and CDK4 in Alzheimer's disease, *Am J Pathol* **1997**, *150*, 1933.

[32] Z. Nagy, M. M. Esiri, A. D. Smith, Expression of cell division markers in the hippocampus in Alzheimer's disease and other neurodegenerative conditions, *Acta Neuropathol* **1997**, *93*, 294.

[33] T. W. Smith, C. F. Lippa, Ki-67 immunoreactivity in Alzheimer's disease and other neurodegenerative disorders, *J. Neuropathol. Exp. Neurol.* **1995**, *54*, 297.

[34] Y. Yang, D. S. Geldmacher, K. Herrup, DNA replication precedes neuronal cell death in Alzheimer's disease, *J. Neurosci.* **2001**, *21*, 2661.

[35] D. J. Bonda, T. A. Evans, C. Santocanale, J. C. Llosa, J. Vina, V. P. Bajic, R. J. Castellani, S. L. Siedlak, G. Perry, M. A. Smith, H.-g. Lee, Evidence for the progression through S-phase in the ectopic cell cycle re-entry of neurons in Alzheimer disease, *Aging* **2009**, *1*, 382.

[36] J. Woods, M. Snape, M. A. Smith, The cell cycle hypothesis of Alzheimer's disease: Suggestions for drug development, *Biochim. Biophys. Acta, Mol. Basis Dis.* **2007**, *1772*, 503.

[37] S. R. D'Mello, P. C. Chin, Treating neurodegenerative conditions through the understanding of neuronal apoptosis, *Curr. Drug Targets CNS Neurol. Disord.* **2005**, *4*, 3.

[38] E. A. Monaco, III, M. L. Vallano, Role of protein kinases in neurodegenerative disease: cyclin-dependent kinases in Alzheimer's disease, *Frontiers in Bioscience* **2005**, *10*, 143.

[39] A. Beauchard, H. Laborie, H. Rouillard, O. Lozach, Y. Ferandin, R. Le Guevel, C. Guguen-Guillouzo, L. Meijer, T. Besson, V. Thiery, Synthesis and kinase inhibitory activity of novel substituted indigoids, *Bioorg. Med. Chem.* **2009**, *17*, 6257.

[40] R. Akue-Gedu, E. Debiton, Y. Ferandin, L. Meijer, M. Prudhomme, F. Anizon, P. Moreau, Synthesis and biological activities of aminopyrimidyl-indoles structurally related to meridianins, *Bioorg. Med. Chem.* **2009**, *17*, 4420.

histidine complexes were shown to involve equilibrating square pyramid and square planar structure with 2:1 histidine-Cu(II) stoichiometry.[31]

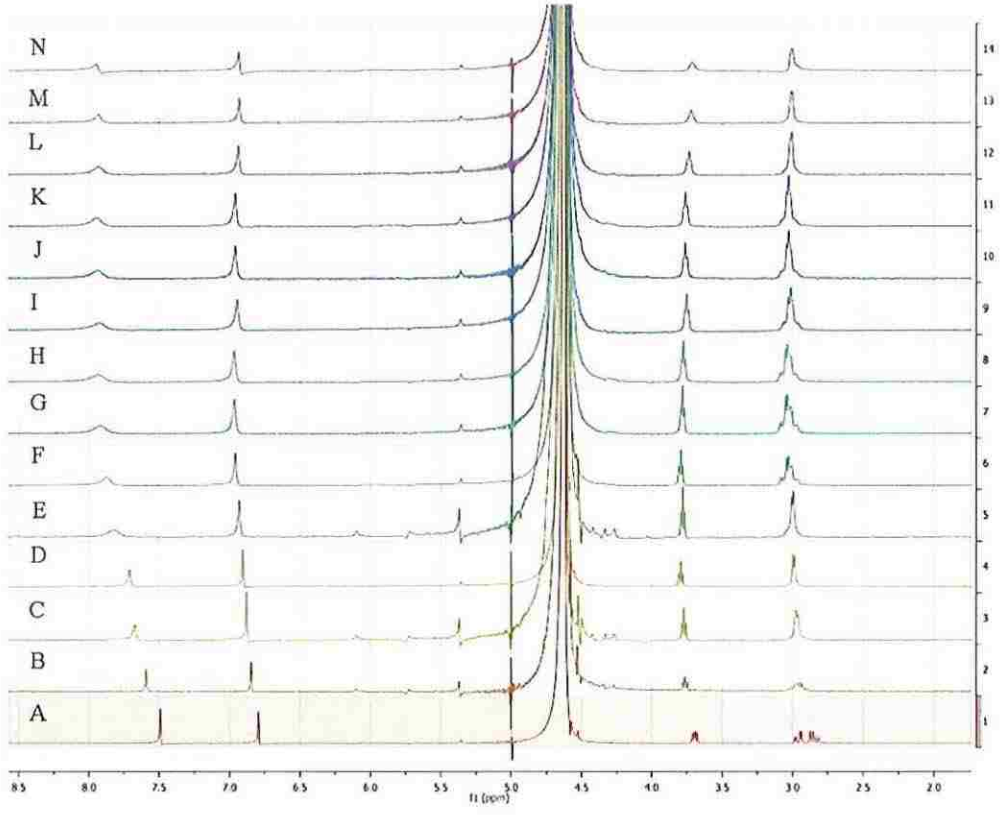

Figure 2.1. ^{1}H NMR titration of histidine with Zn(II) in D_2O (δ^1H (D_2O) = 4.63ppm) solution at 25 °C and at a pH of 7.45 ± 0.01. Spectrum A is for histidine dissolved in phosphate buffered D_2O (pH 7.45); spectra B to N are for incremental additions of Zn (II) to histidine solution (A); in each of these later solutions the [Zn(II)] / [histidine] ratios are as follows: B, 0.05; C, 0.10; D, 0.15; E, 0.2; F, 0.31; G, 0.52; H, 0.73; I, 1.04; J, 1.25; K, 1.41; L, 1.99; M, 3.91; N, 5.75. The absorption at δ^1H 7.49 corresponding to imidazole-2H was relatively most deshielded indicating strong binding of histidine through imidazole-N3. From the spectral changes it is evident that other binding sites of histidine are the amino and carboxyl groups.

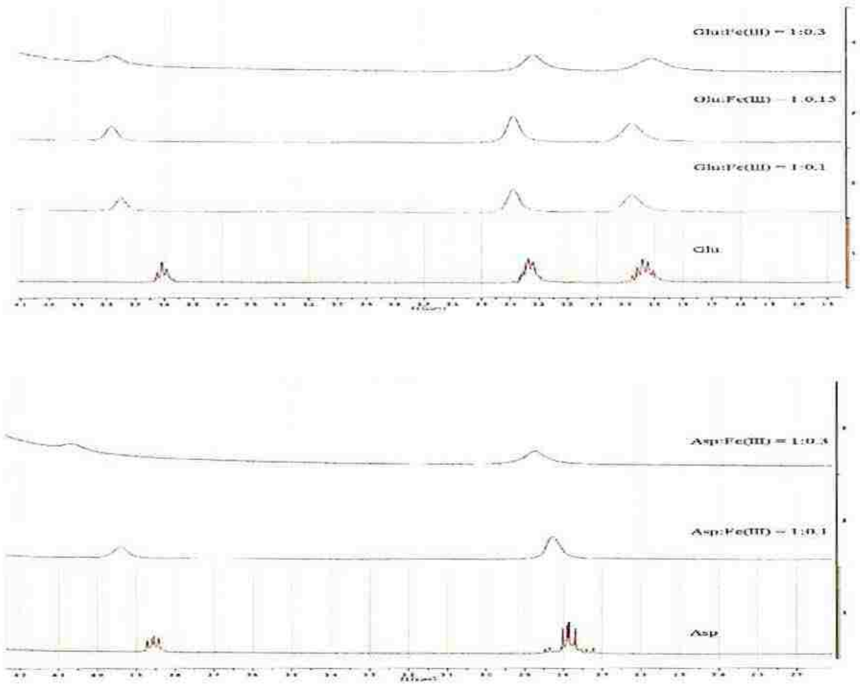

Figure 2.6. ^{1}H NMR spectra of glutamic acid/Fe(III) (top) and aspartic acid/Fe(III) (bottom). Addition of up to 0.3 mol equivalents of Fe(III) to glutamic acid and aspartic acid resulted in relatively minor deshielding of the chemical shifts, as compared to histidine, showing relatively weak binding affinity of these amino acids with Fe(III).

2.2.3 Conclusion. As a model to the metal ion binding to Aβ peptide, we have investigated the relative binding efficiencies of Fe(III), Cu(II), and Zn(II) to histidine, tyrosine, aspartic acid and glutamic acid using ^{1}H NMR titration experiments. From the observed deshielding of the chemical shifts it is evident that histidine is the major binding site for the metal ions. We have found a stoichiometry of Zn:histidine of 1:2, suggesting an octahedral structure to the complex. From NMR titration experiments it can be concluded that the Fe(III)/Fe(II) and Cu(II) bind relatively more strongly than Zn(II) to histidine.

Thus the total volume of each of the solutions is kept constant at 2.5 mL, and the sum of the moles of the Cu(II) and the antioxidant for each of these solutions was also constant (5 x 10^{-5} moles), as required for the continuous variation method. The absorption at 800 nm, for the Cu(II) species, was shifted to lower wavelengths upon successive additions of the aliquots of the antioxidants, histidine and carnosine. The absorption maxima for the complexed species were observed between 350 to 1000 nm (Figure 3.2 and 3.3).

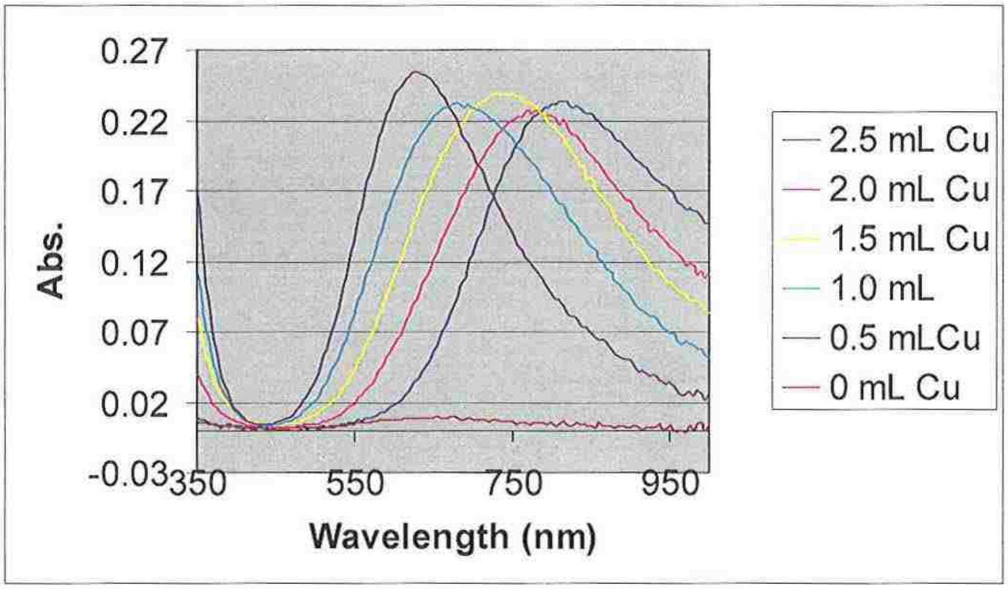

Figure 3.2. UV/vis absorbance of L-Histidine-Cu(II) complex

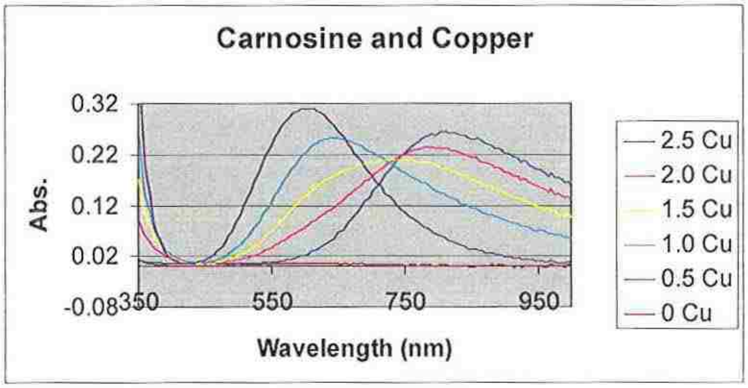

Figure 3.3. UV/vis absorbance of L-Carnosine-Cu(II) complex

The absorbances at a fixed wavelength (800 nm in case of carnosine and 810 nm in case of histidine) were then recorded at different mole fractions (represented as X in Figures 3.4 and 3.5) of Cu(II), and the changes in absorbance of the Cu(II) ion complexes as compared to the uncomplexed Cu(II) species were calculated from these spectra.

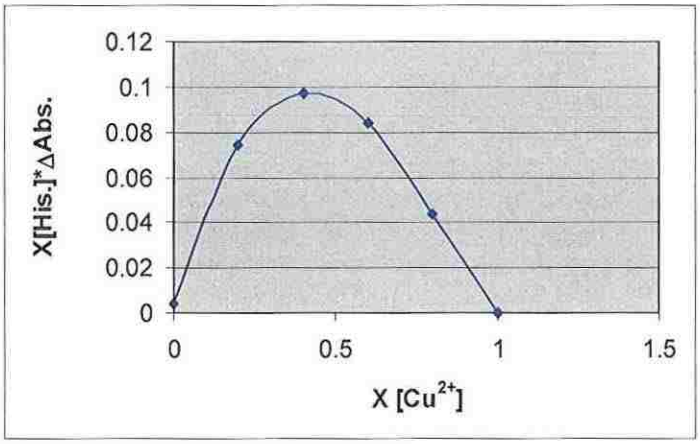

Figure 3.4. Job's plot for L-Histidine-Cu(II) complex

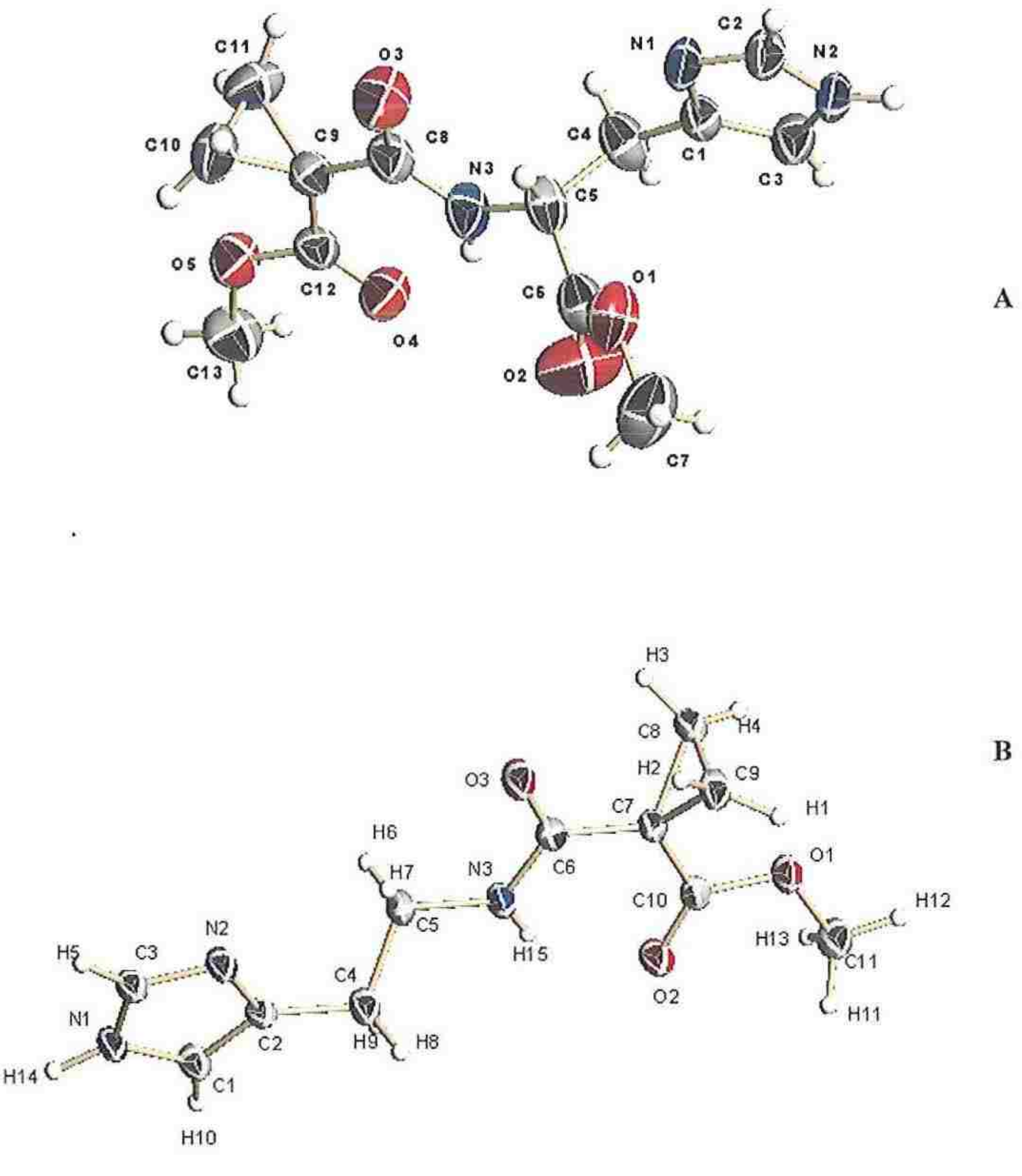

Figure 3.9. Single crystal X-ray structure of N-(α)-((1-mehoxycarbonyl)cyclopropylcarbonyl)histamine (2) (B) and N-(α)-((1-mehoxycarbonyl)cyclopropylcarbonyl)histidine (1) (A)

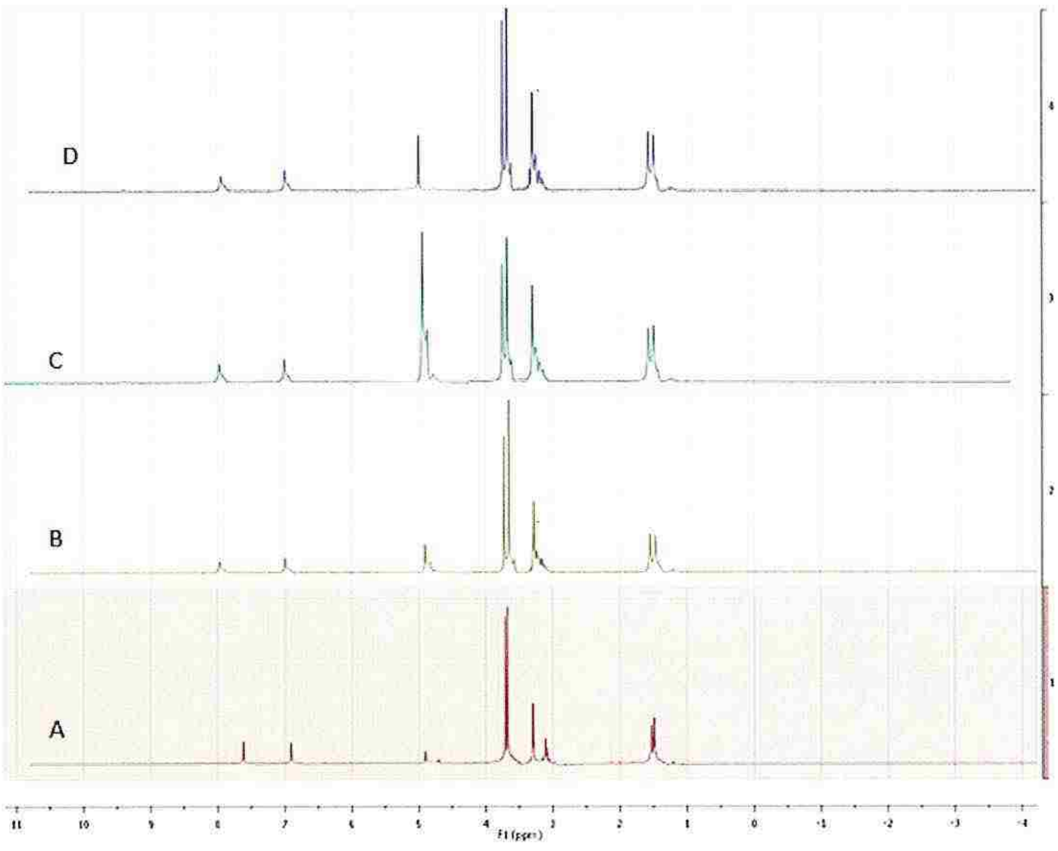

Figure 3.13. ^{1}H NMR titration of N-(α)-((1-mehoxycarbonyl)cyclopropylcarbonyl)histidine (N-(α)-((1-mehoxycarbonyl)cyclopropylcarbonyl)histidine) with Zn(II) in Methanol-*d*. Spectrum A is for N-(α)-((1-mehoxycarbonyl)cyclopropylcarbonyl)histidine in Methanol-*d* solution; spectra B-D are for incremental additions of Zn(II) to solution of N-(α)-((1-mehoxycarbonyl)cyclopropylcarbonyl)histidine (A). In each of these later solutions the [Zn(II)]/ [N-(α)-((1-mehoxycarbonyl)cyclopropylcarbonyl) histidine ratios are as follows; B, 0.2; C, 0.5; D, 2.

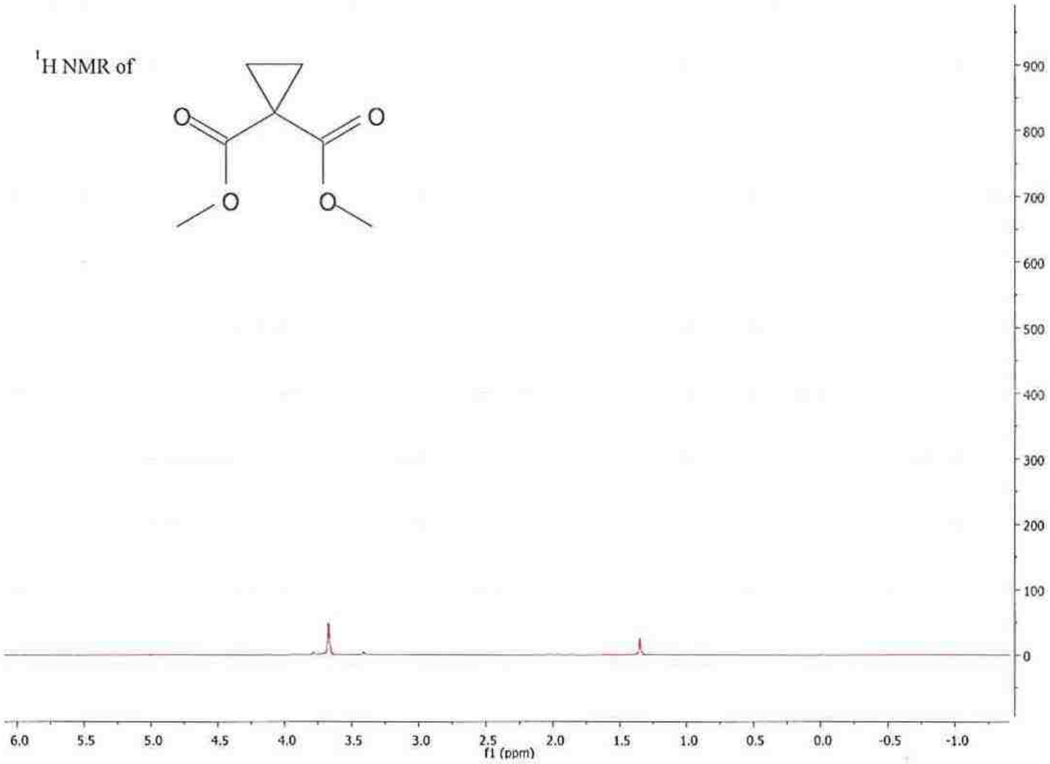

Figure 3.14 ^{1}H NMR (400MHz) spectrum of Dimethyl 1,1.cyclopropanedicarboxylate (5a)

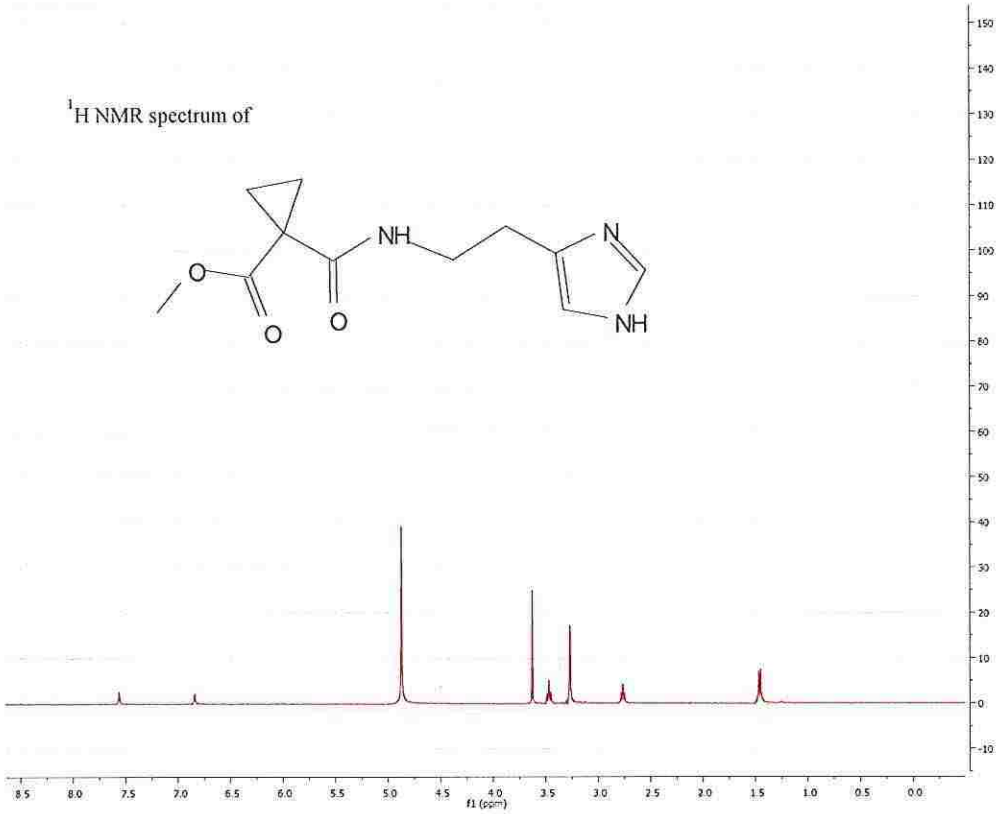

Figure 3.15. ^{1}H NMR (400MHz) spectrum of N-(α)-((1-mehoxycarbonyl)cyclopropylcarbonyl)histamine

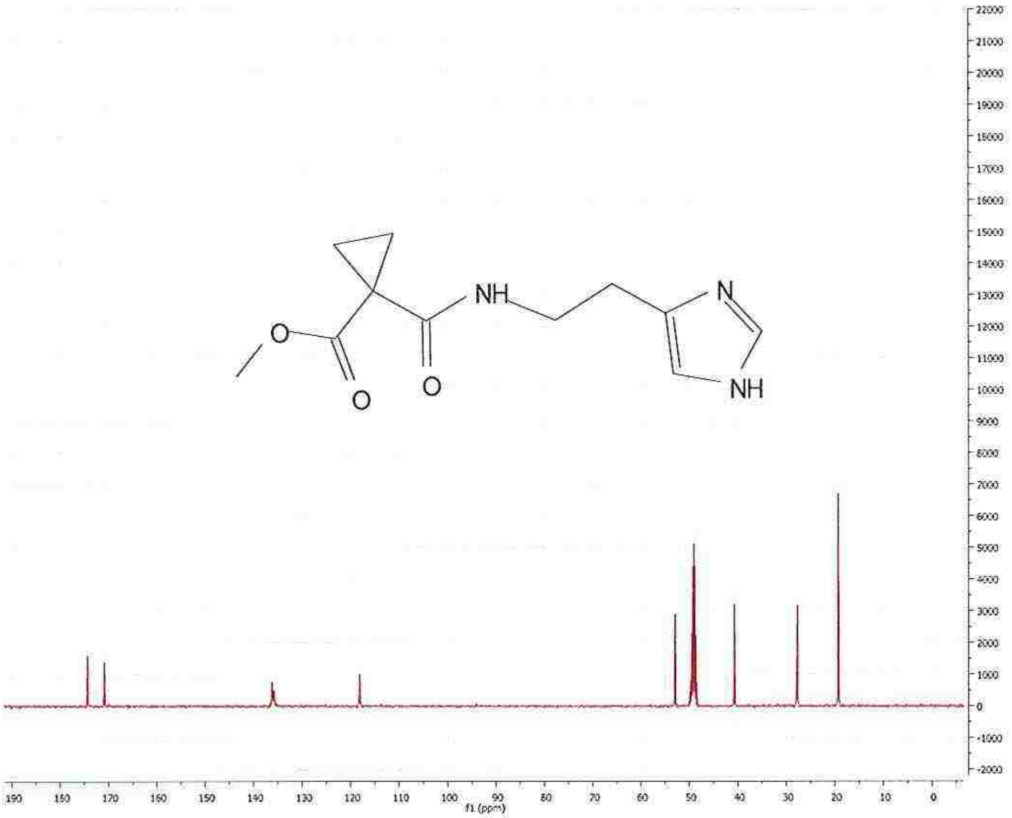

Figure 3.16. ^{13}C (100MHz) NMR spectrum of N-(α)-((1-mehoxycarbonyl)cyclopropylcarbonyl)histamine.

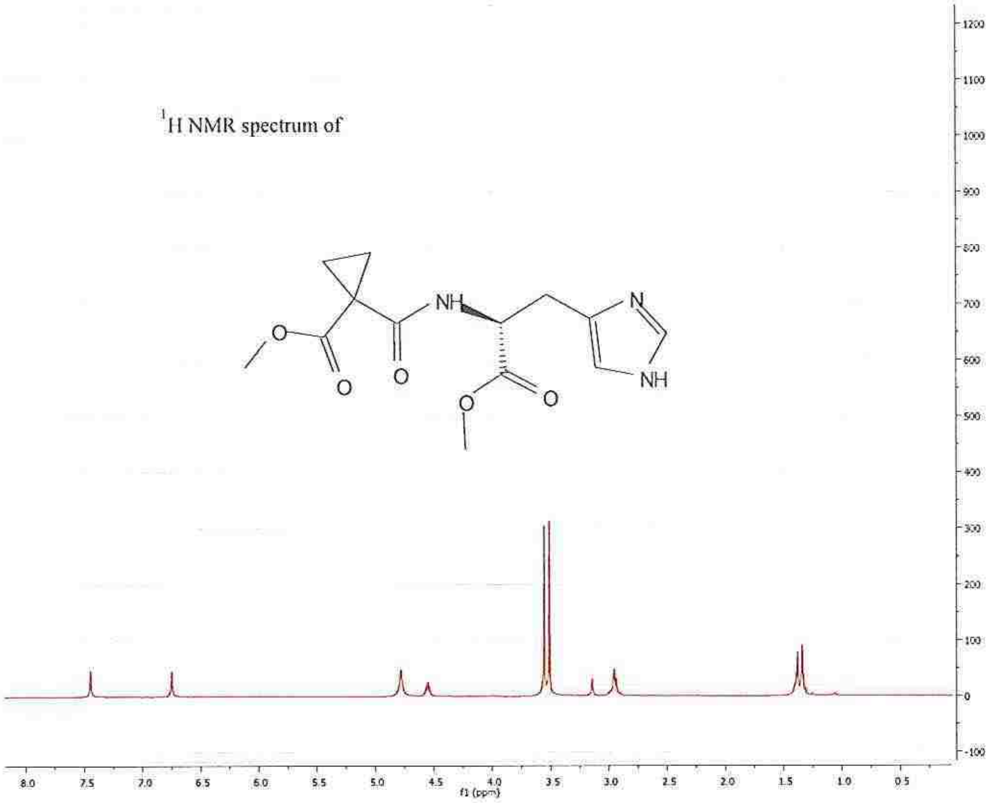

Figure 3.17. ¹H (400 MHz) NMR spectrum of N-(α)-((1-mehoxycarbonyl) cyclopropylcarbonyl)histidine

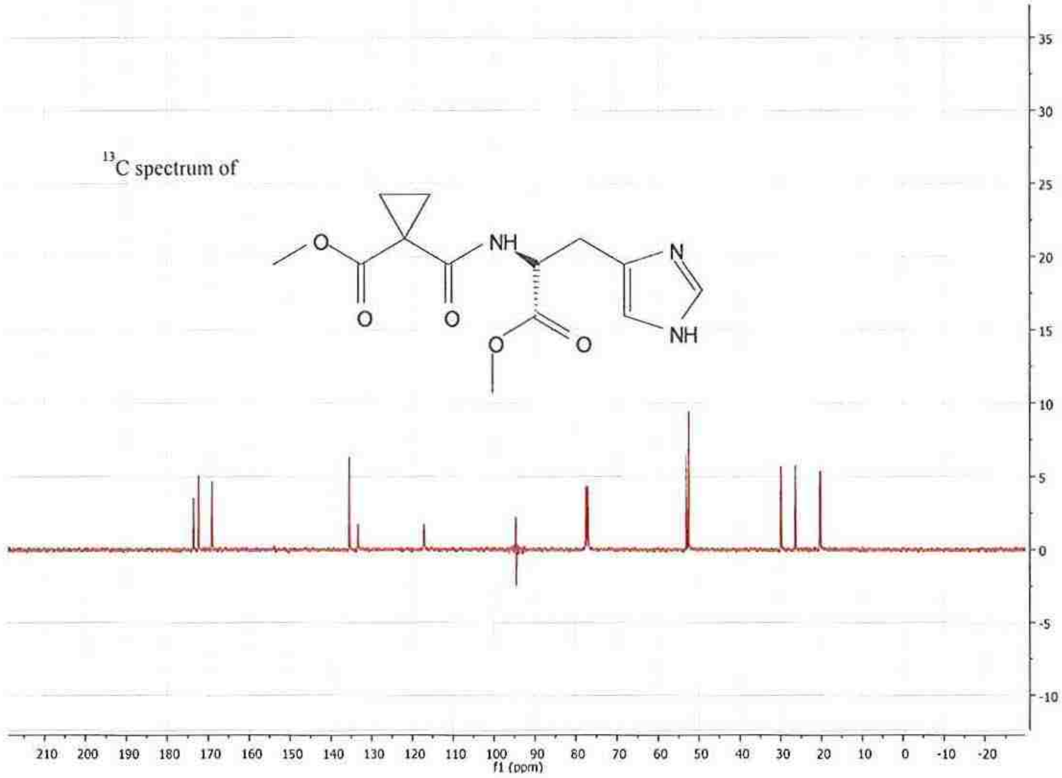

Figure 3.18. ^{13}C (100MHz) NMR spectrum of N-(α)-((1-mehoxycarbonyl) cyclopropylcarbonyl)histidine.

3.2.4.2 Single crystal X-ray crystallographic analysis. *Crystal Structure Analysis of compound 1:* Data collection: Bruker Instrument Service v2009, 3, 0, 0; cell refinement: *APEX2* v2009.3.0 (Bruker AXS); data reduction: *SAINT* V7.60A (Bruker AXS, 2008); program(s) used to solve structure: *SHELXS97* (Sheldrick, 2008); program(s) used to refine structure: *SHELXL97* (Sheldrick, 2008).

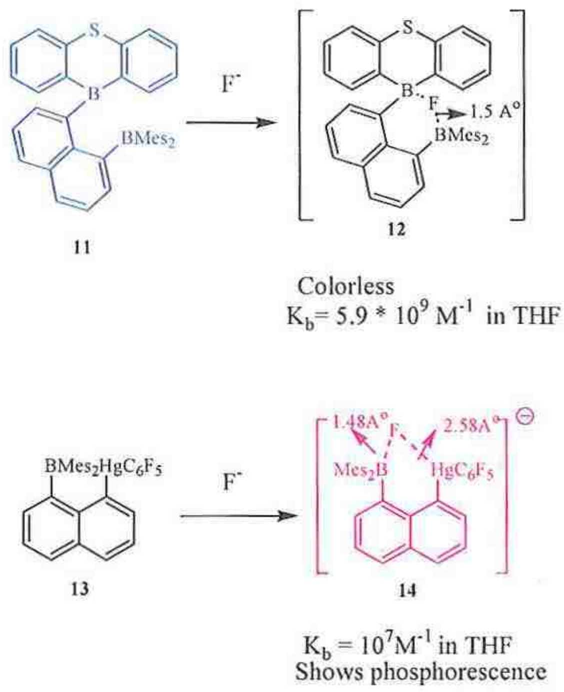

Colorless
$K_b = 5.9 * 10^9\ M^{-1}$ in THF

$K_b = 10^7 M^{-1}$ in THF
Shows phosphorescence

Scheme 4.3. Examples of bidentate Lewis acids as Colorimetric and Phosphorescent Fluoride Sensor.

All of these bidentate anion receptors for fluoride, as discussed above are limited to organic solvents. Due to the importance of detection of fluoride ions in water, Hudnall and coworkers developed cationic boranes, involving quaternary ammonium and phosphonium groups (15, 16 and 17) for fluoride anion binding in aqueous solutions (Figure 4.2). [12] However, their binding constants with fluoride are less than their related bidentate anion receptors. More importantly, compounds 15 and 17 are selective for fluoride anion, whereas para-substituted compound 16 is relatively more selective for cyanide anions.

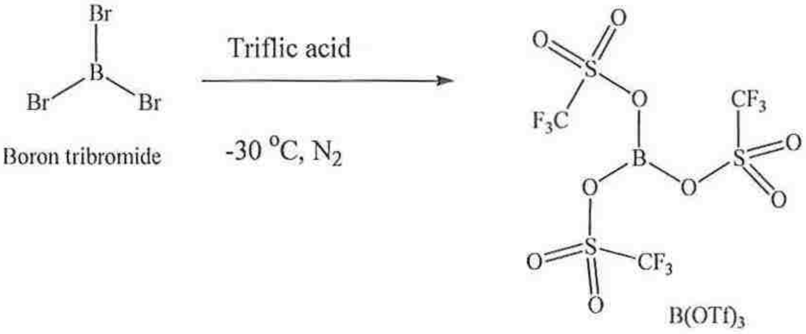

Scheme 4.5. Synthesis of Boron tris(triflate) (B(OTf))

NMR analysis of the $B(OTf)_3$ showed that it forms adducts with solvents such as dimethyl sulfoxide (Figure 4.5) and acetonitrile (Figure 4.6). Triaryl boranes are known to form solvent adducts with acetonitrile.[14]

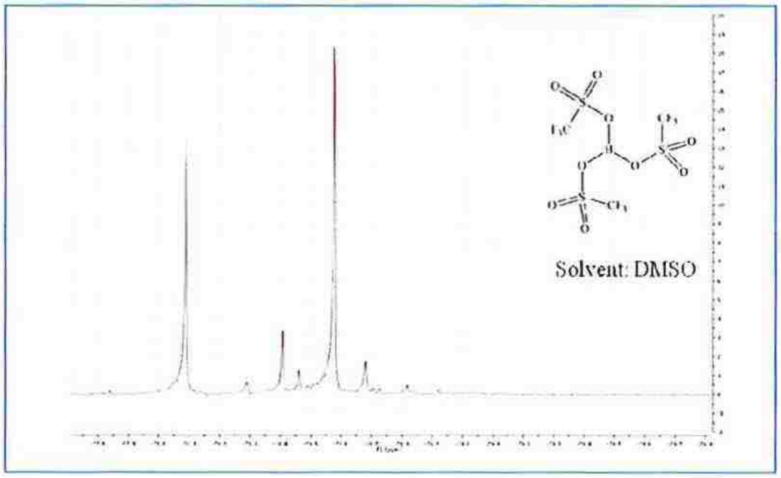

Figure 4.5. ^{19}F NMR of borontristriflate in DMSO.

In acetonitrile solution three ^{19}F peaks peaks were observed at -78.55 (B), -78.39 (C) and -78.09 (D) ppm (Figure 4.7). In order to investigate whether any of the peaks correspond to triflic acid, increasing amount of triflic acid (100 μL) was added to the solution of boron tris(triflate) in acetonitrile . On addition of triflic acid a new peak emerged at -77.7 ppm corresponding to triflic acid which was verified by adding extra amounts of triflic acid (Figure 4.6). The unidentified peaks may correspond to solvent adducts of Boron tris(triflate). Thus boron tris(triflate) is not a suitable candidate for stduying fluoride ion binding due to its moisture sensitivity and reactivity with solvents.

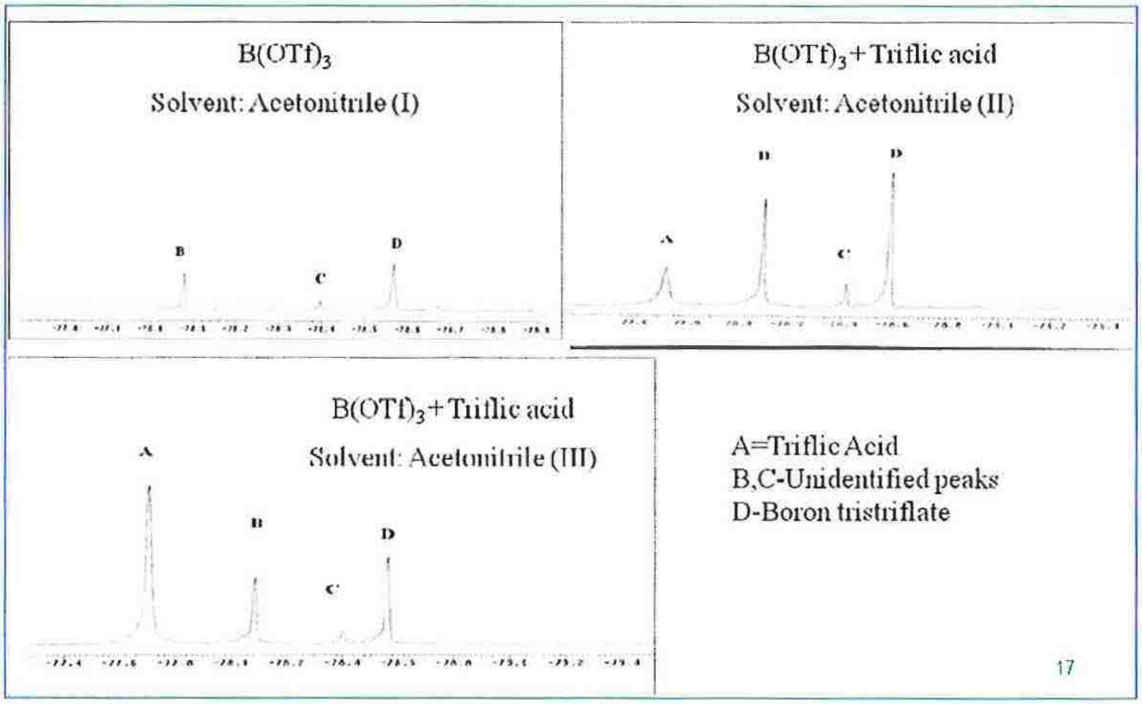

Figure 4.6. ^{19}F NMR of boron tris(triflate) in acetonitrile.

Similarly with DMSO there were three larger peaks at δ 75.1, 75.4 and 75.5 (Figure 4.7). Due to its intrinsic Lewis acidity it may be forming adducts with nucleophilic solvents. It was also found that BTTA polymerizes THF solvent in accordance with the literature reports.[16]

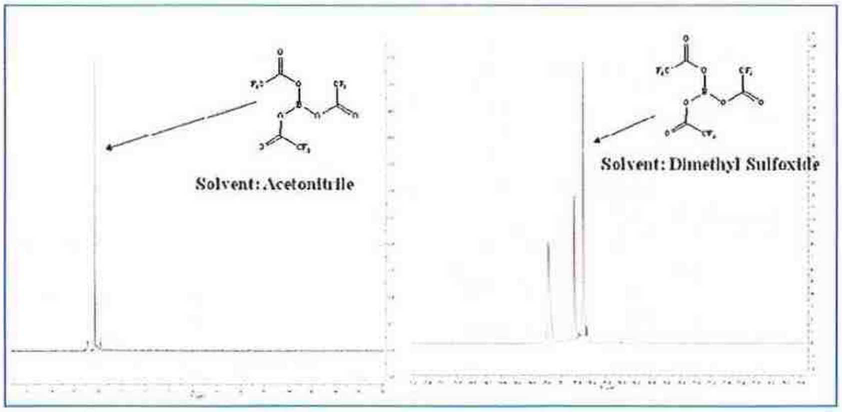

Figure 4.7. ^{19}F NMR of BTTA in acetonitrile (left) and dimethylsulfoxide(right).

In order to determine the fluoride ion binding affinity, BTTA was titrated with, tetrabutyl ammonium fluoride (1.2 equivalents) in acetonitrile and DMSO (Scheme 4.7). NMR analysis of the resultant solution shows that on addition of fluoride ion additional peaks were formed in the range of δ -75.62 to -76.32ppm in acetonitrile and other solvents. UV-Vis spectroscopic titrations also indicated the formation of multiple equilibria. Thus BTTA is not a suitable compound for fluoride ion binding studies using NMR or UV spectroscopy.

ortho-fluorines, upfield by 5 ppm for *para*-fluorines, and upfield by 2 ppm for the *meta*-fluorines.

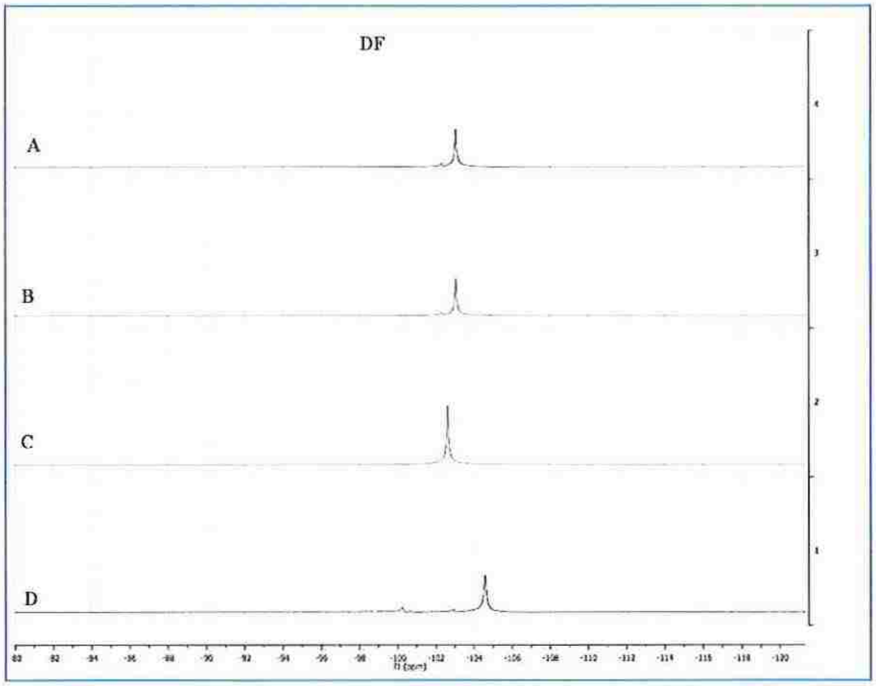

Figure 4.11. ^{19}F NMR spectra of DF (4) in CH_3CN (A), EtOAc (B), DMSO (C), and CH_2Cl_2

The ^{19}F NMR of PF, TF and DF in various solvents thus clearly show the importance of solvation. In case of TF and DF there is rapid exchange of the solvent molecules among the three boron centers of the complex so that only a single ^{19}F NMR absorption is observed for the all the aromatic ortho or *para* fluorines. However, in relatively more polar DMSO solvent, additional distinct absorptions for PF-DMSO adducts could be observed. This indicates relatively slow exchange of the DMSO with

PF. Unlike the starting boroxines, the boroxin-fluoride adducts (in the presence of excess fluoride anion) have similar $\delta^{19}F$ in all the solvents studied (CH_2Cl_2, acetonitrile, and DMSO), showing that the solvent participation is minimal in the case of the fluoride adducts.

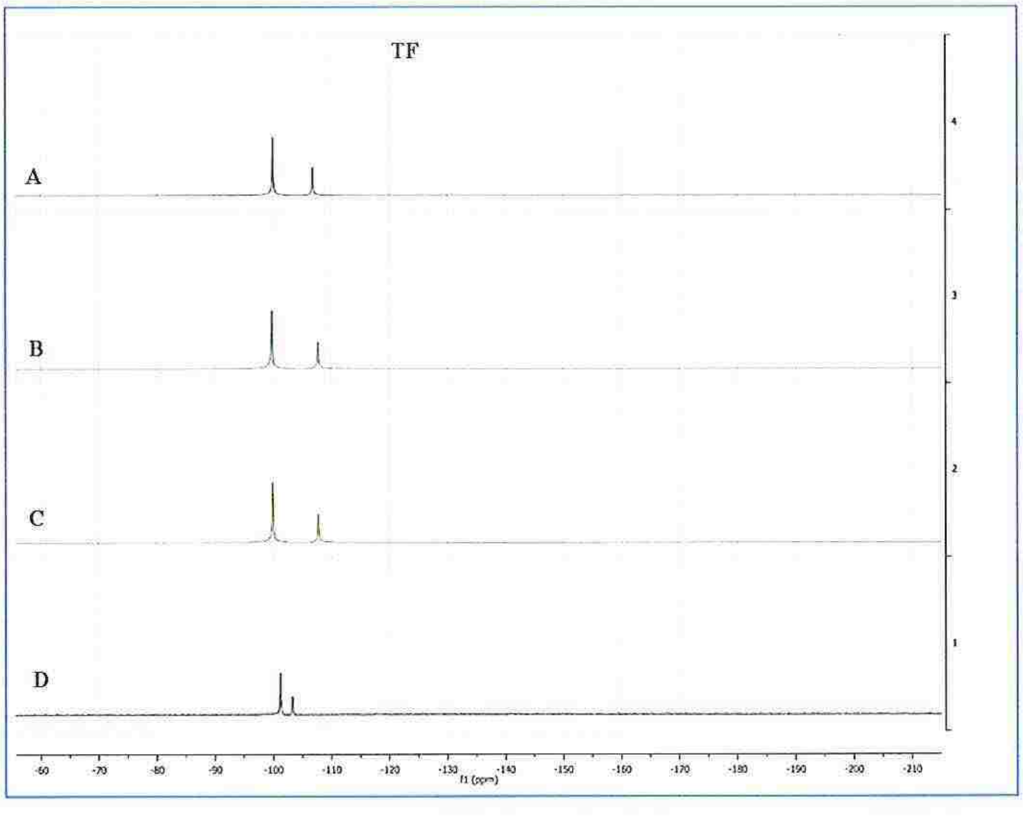

Figure 4.12. ^{19}F NMR spectra of TF (5) in CH_3CN (A), EtOAc (B), DMSO (C), and CH_2Cl_2

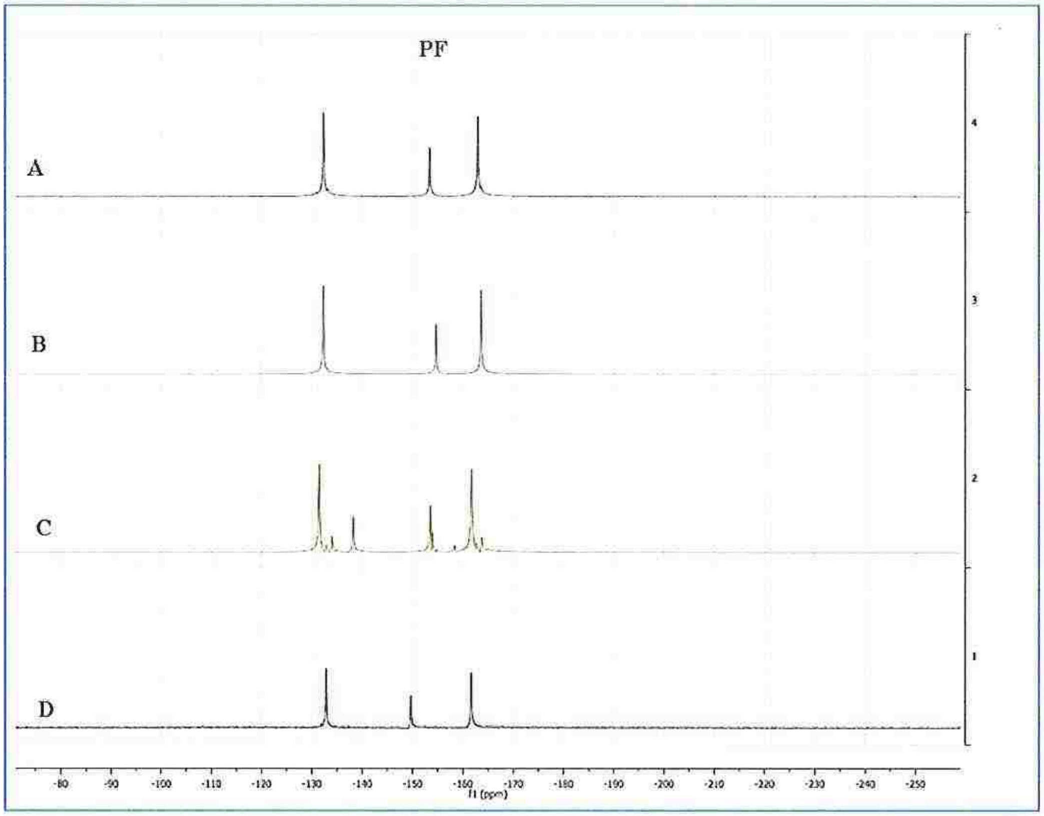

Figure 4.13. ^{19}F NMR spectra of PF (6) in CH_3CN (A), EtOAc (B), DMSO (C), and CH_2Cl_2

4.3.4 Fluoride Anion Binding. Fluoride anion binding to anion receptors helps not only the solubility of the otherwise insoluble lithium fluoride electrolyte in nonaqueous organic solvents, but also dramatically increases the lithium ion conductivities. Reversibility of fluoride anion binding is crucial in the next generation dual ion intercalating lithium ion batteries. In order to understand the structural effects on the fluoride binding to anion receptors we carried out DFT calculations on a series of fluorinated boroxines, and the results are shown in Table 4.2 and Figure 4.14. As can be

absorptions corresonding to the starting PF could not be observed even after addition of one mol equivalent of TBAF. The *ortho-* fluorines are relatively more shielded in the PF-fluoride complex (28) as compared to the *meta-* and *para*-fluorines, as expected due to the proximity of the negatively charged boron.

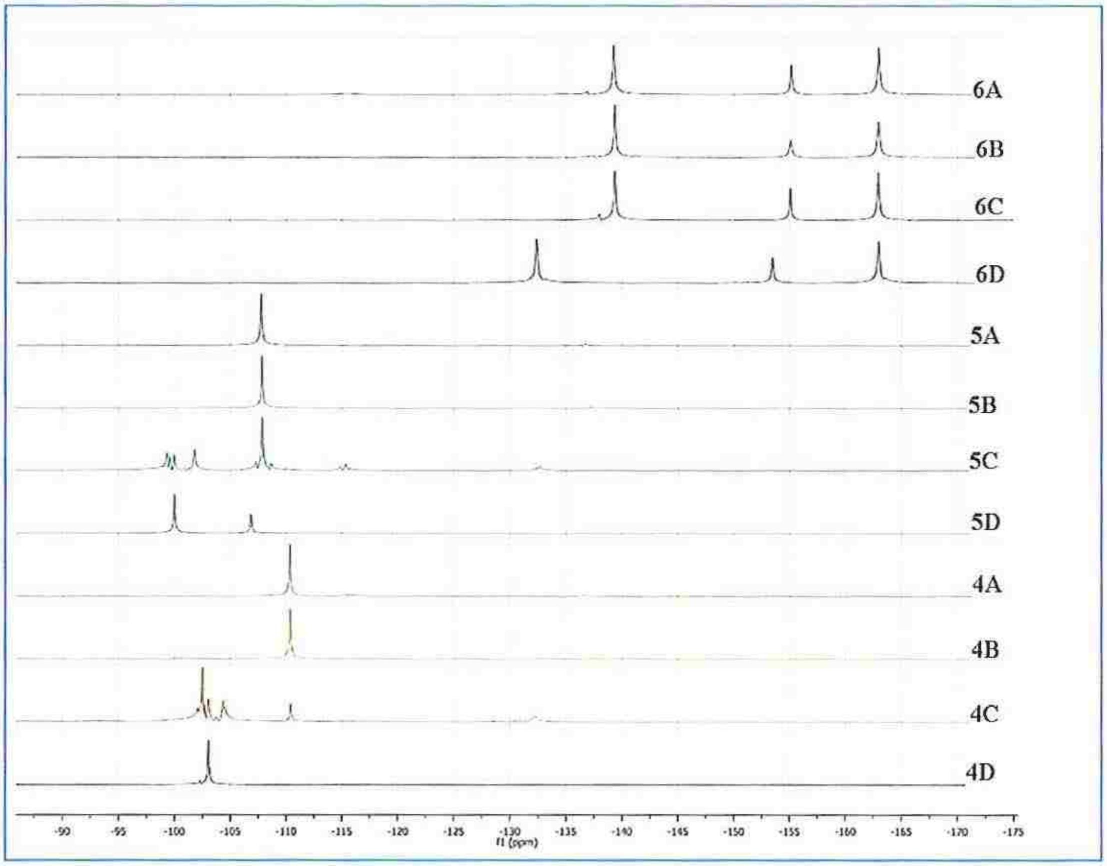

Figure 4.16. ^{19}F NMR (376MHz) spectra of DF (23), TF (24), and PF (25) in acetonitrile at various molar equivalents of TBAF: boroxin : TBAF = 1:3 (A); boroxin : TBAF = 1:2 (B); boroxin : TBAF = 1:1 (C); boroxin without added TBAF (D).

4.3.5 ^{11}B NMR Studies and GIAO Calculations. The ^{11}B NMR for the fluoride complexes (26, 27, and 28) are shown in Figure 4.17. DF-fluoride complex (26) shows two ^{11}B absorptions at δ^{11}B 19.8 (sp^2·B) and 1.2 (sp^3·B). TF-fluoride complex and PF-fluoride complexes similarly show two ^{11}B absorptions: δ^{11}B (TF): 20.1 (sp^2·B) and 1.2 (sp^3·B); δ^{11}B (PF): 20.4 (sp^2·B) and 1.2 (sp^3·B). The DFT-GIAO derived chemical shifts are in reasonably close agreement ($\Delta\delta = 2.8$ to 5.9) with experimental values so that the assignments of the ^{11}B absorptions in the complexes could be confirmed.

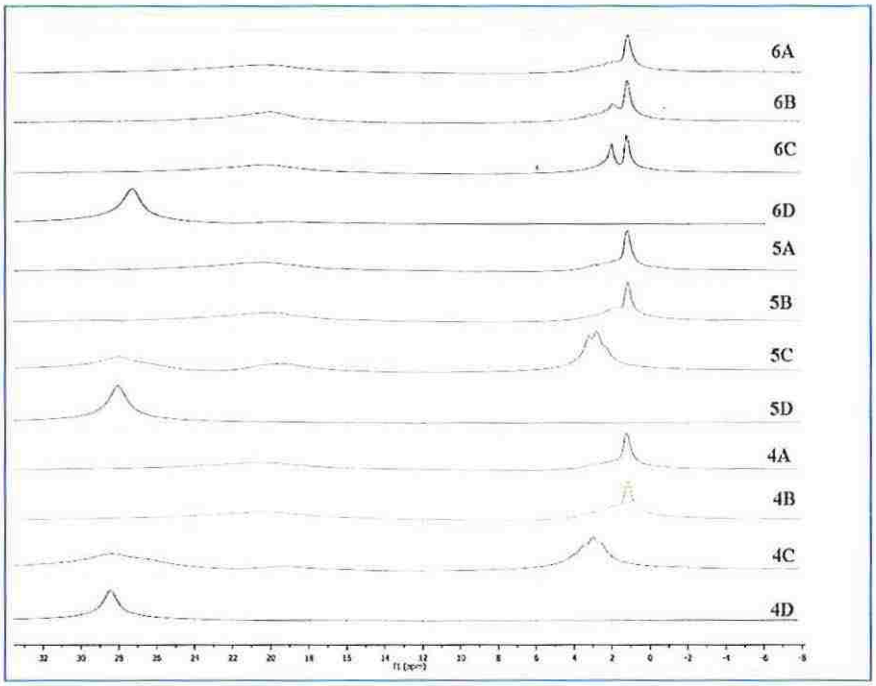

Figure 4.17. ^{11}B NMR (128 MHz) spectra of DF (23), TF (24), and PF (25) in acetonitrile at various molar equivalents of TBAF: boroxin : TBAF = 1:3 (A); boroxin : TBAF = 1:2 (B); boroxin : TBAF = 1:1 (C); boroxin without added TBAF (D).

UV-Vis spectra were recorded for a series of DF/TBAF (PF/TBAF) solutions; the mol ratios of DF to fluoride (PF to fluoride) were continually varied while keeping the total concentration of each of their solutions constant. The measured UV-vis absorbances at 265, 265, 260, and 64 nm (multiplied by mol fraction of boroxines) were plotted against mol fractions of the TBAF (Figure 4.18).[36-37] Through these Job's plots, stoichiometry of the DF-fluoride complex was determined as 1:1. In case of DF 1:1 stoichiometry is consistently observed at all wavelengths: 269, 265, 260, and 64 nm (Figure 4.18B) Stoichiometry of host-guest complexation is independent of UV-vis wavelength in Job's plots, if a single complex is formed. On the other hand, dependence of Job's maxima on wavelength is indicative of the co-existence of more than one complex.[35],[38-39] The Job's plots for PF, show deviations from 1:1 stoichiometry at different wavelengths, indicating the possible co-existence of more than one complex for PF (Figure 4.18C) (*vide supra*).

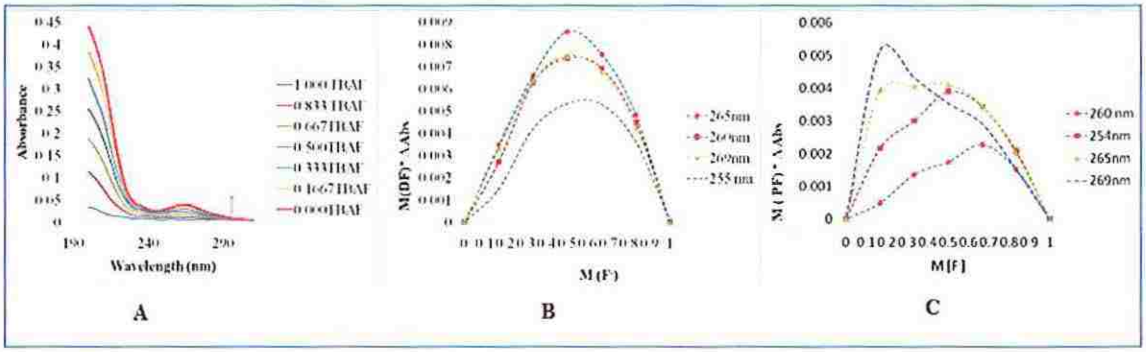

Figure 4.18. UV-Vis Spectra (in acetonitrile) obtained from continuous variation method (A), and Job's plots for DF(B) and PF(C); B and C are the overlay plots for absorbances at 269, 265, 260 and 65 nm.

complex, 26, shows significantly upfield shifted ^{19}F signals for the fluorine atoms attached to aromatic rings. However, we were not able to observe the absorptions corresponding to the fluoride anion attached to boron.

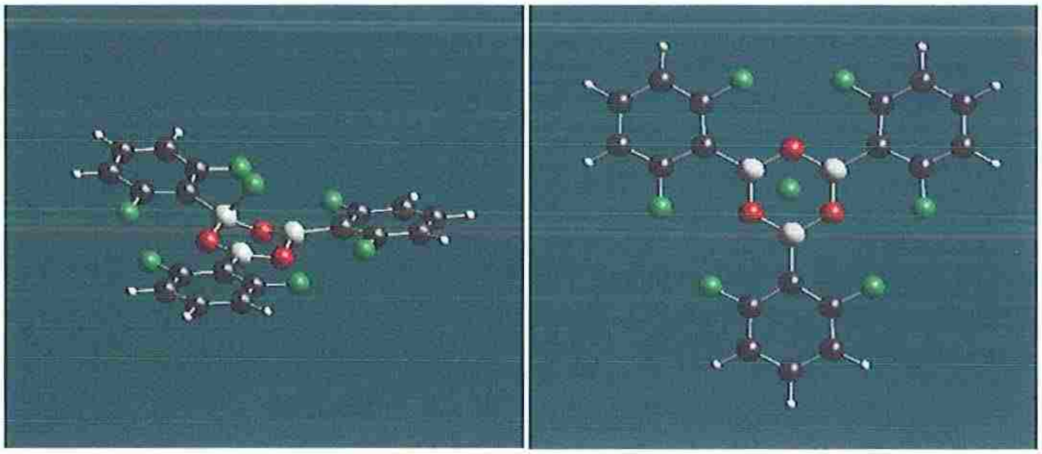

Figure 4.20. B3LYP/6-311G** structures of asymmetic and symmetrically bridged [DF-F]$^-$ complexes, corresonding to structures 26 (left) and 29 (right).

The lack of detection of the boron-bound fluoride absorption indicates that there is rapid equilibrium between three unsymmetrical structures relative to the NMR time scale at ambient temperature with an estimated free energy of activation of 12.0 to 12.5 kcal/mol (*vide supra*). Geometries for the PF and [PF-F]$^-$ are shown in (Figure 4.21). In the neutral form the PF anion receptor is a propeller shape molecule with a small angle (36.4 degrees) between the boroxin ring and the phenyl groups. In the charged state [PF-F]$^-$ the boron atom that captures the fluoride anion becomes more tetragonal and the propeller angle increases significantly (79.7 degrees).

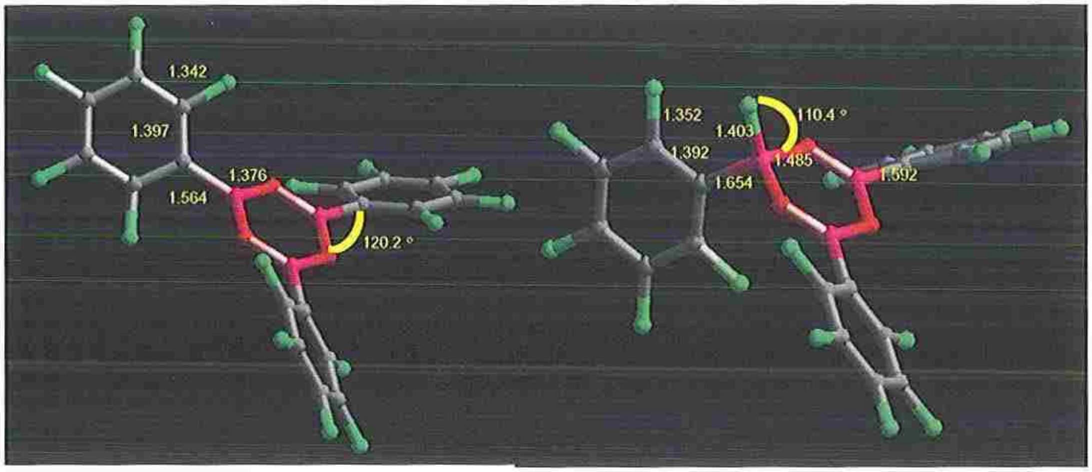

Figure 4.21. B3LYP/6-311G** solution (propylene carbonate) geometry-optimized structures of neutral PF (left) and the corresponding charged $[PF\text{-}F]^-$ complex (right).

4.3.8 Tandem Mass spectroscopic Studies of Boroxin Fluoride Complex. In light of the importance of the selective binding of the electrolyte materials to the anion receptors, it is useful to characterize the structural details of the boroxin-anion complexes. Electrospray ionization mass spectroscopy in the negative ion mode is ideally suited for characterization of the stoichiometry of the fluoride anion complexes.[41-42] Competitive ESI-MS studies also would provide quantitative information on the relative bidning affinities. Further, the tandem mass spectrometric fragmentations would reveal the mechanistic aspects of the rearrangements involved in the fragmentations. We now report the electrospray mass spectrometric characterization of the molecular ion complexes for these fluorinated boroxines, also substantiated by the DFT studies. Electrospray ionization mass spectroscopy (ESI-MS) is expected to show the molecular ion peaks for the boroxin anion complexes, and thus direct characterization of the anion complexes could be achieved. The molecular ion peaks for the fluoride anion adducts for DF, TF, and PF, corresponding to m/z of 439, 493 and 601, respectively were observed. The observed isotopic ratios for MF-2, MF-1, MF, and MF+1 for DF-F$^-$, TF-F$^-$, and PF-F$^-$ are generally in accordance with the calculated ratios, confirming these peaks as the molecular ion peaks for the fluoride adducts(Figure 4.22).

Tandem mass spectrometry is useful in the characterization of the fragmentation mechanisms. The fragmentation mass spectrum obtained by the collision induced dissociation (CID) of the DF-fluoride (26) molecular ion peak at 439 showed appearance of the peaks at m/z 345, 61, 113 (Figure 4.23). These m/z values could be readily assigned to the anion species 26a, 26b, and 26c arising from the successive eliminations of 3.fluorobenzyne and 1,3,5-trifluoroboroxin, as shown in (Scheme 4.11). Similar fragmentation pattern was observed in case of other boroxines fluoride complexes, TF-F$^-$ and PF- F$^-$.

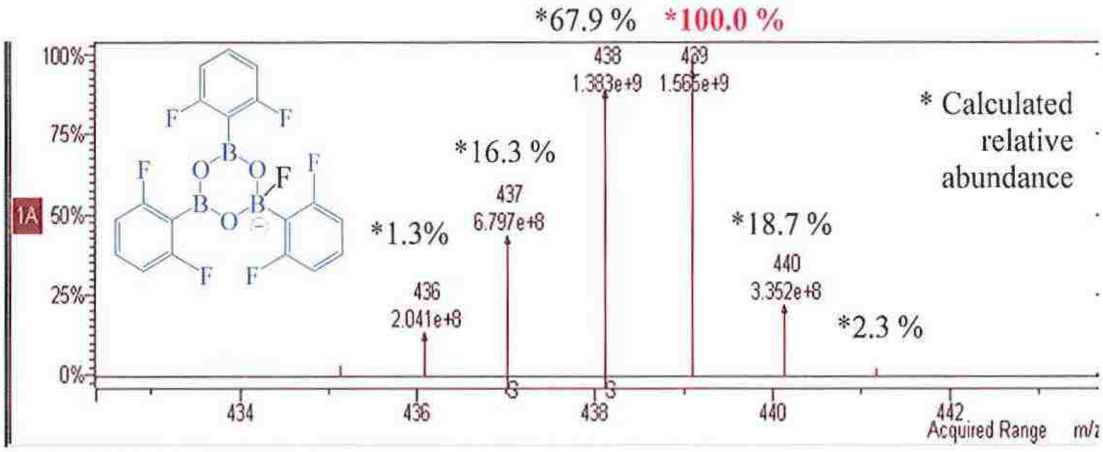

Figure 4.22. Electron spray ionization mass spectrum (ESI/MS) of DF-Fluoride complex showing isotopic pattern.

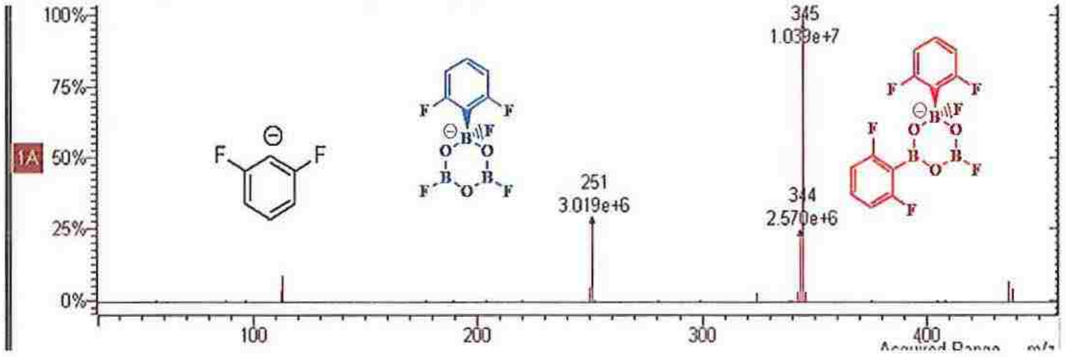

Figure 4.23. ESI/MS spectra showing the molecular ion peaks for the boroxin-fluoride complexes, DF-F⁻, TF-F⁻, and PF-F⁻.

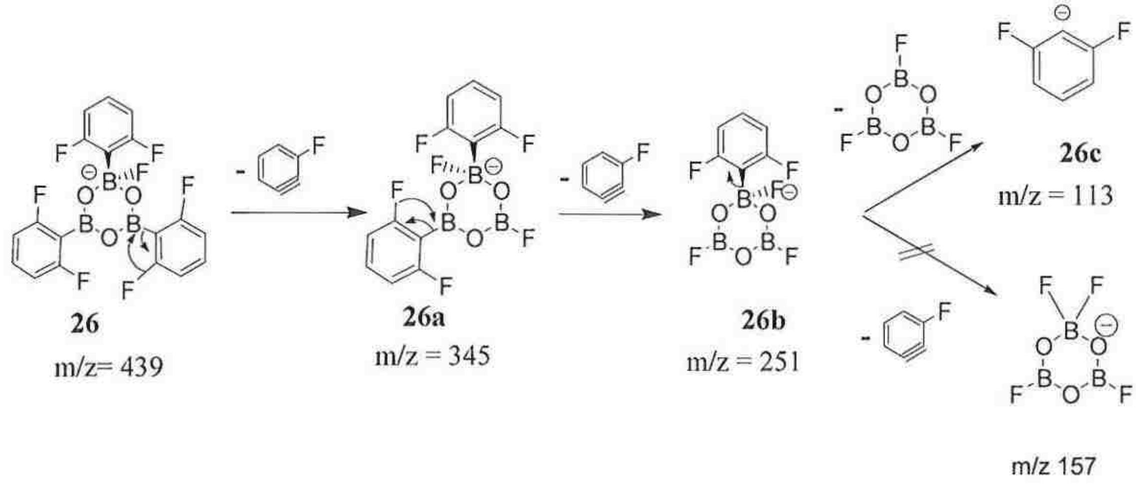

Scheme 4.10. Proposed mechanism for the mass spectral fragmentation of DF-fluoride complex.

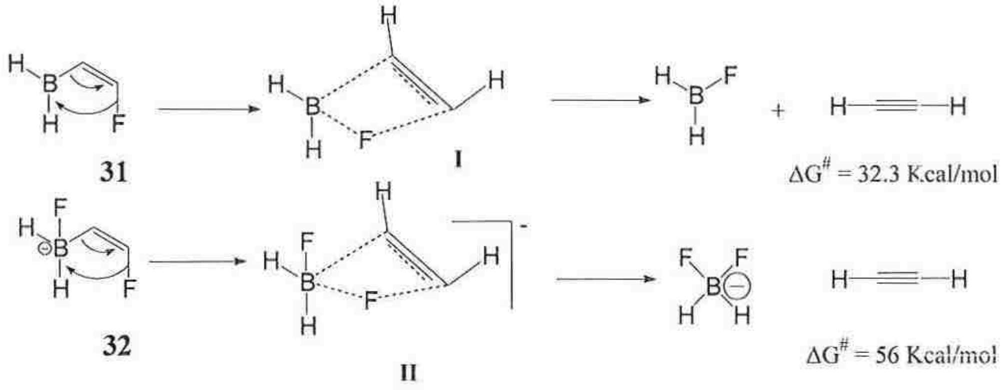

(3)

(4)

Thus expectedly, the 1,3.shift of fluorine to the electrophilic sp^{2}·B (in compound 31) is relatively much faster than that of the sp^{3}·B center (in compound 32). In accordance with these DFT computations, the fragment ion 26b gave anion 26c by the cleavage of the boron-aryl bond, and the corresponding 1,3-sigmatropic fluorine migration was not observed(Scheme 4.11).

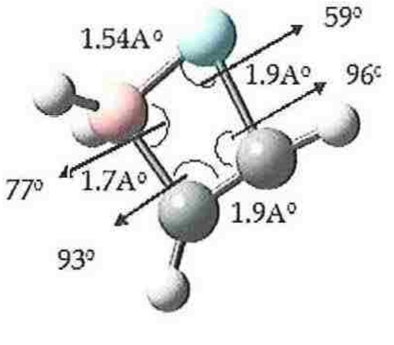

Figure 4-24. Transition state for fluoride migration (II)

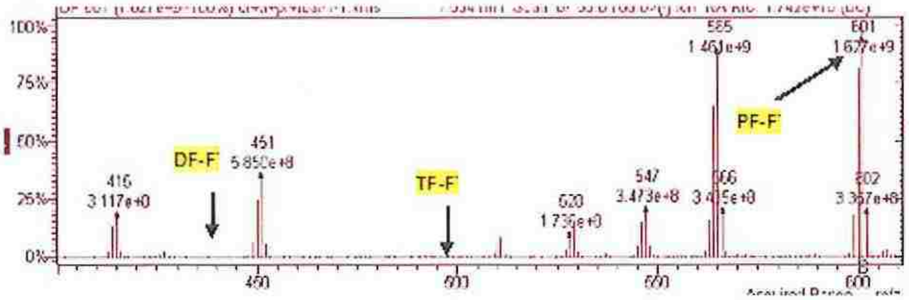

Figure 4.25. ESI/MS spectrum of equimolar mixture of DF, TF and PF in the presence of 0.33 equivalents of TBAF.

Lithium hexafluorophosphate is commonly added as supporting electrolyte in the lithium ion batteries, and therefore it is interesting to compare its relative binding efficiency with anion receptors. It would be also informative to compare the fluoride anion binding strength with that of other commonly used halide anions.

Thus, we have extended these anion binding studies to other halide anions (chloride, bromide, and iodide anions), and hexafluorophosphate. When each of these boroxines was separately mixed with TBACl, TBABr, TBAI, and $TBAPF_6$ and subjected to negative ion ESI mass spectrometry, we have not been able to observe the corresponding molecular ion peaks for the anion adducts(equation 7, 8 and 9, (No detectable MX]- peaks) in ESI-MS).

$$\mathrm{DF} \; \cancel{\xrightleftharpoons[X\, =\, Cl^-,\, Br^-,\, PF_6^-]{BuN^+X^-}} \; \mathrm{DF\text{-}X]^-} \qquad (7)$$

$$\mathrm{TF} \; \cancel{\xrightleftharpoons[X\, =\, Cl^-,\, Br^-,\, PF_6^-]{BuN^+X^-}} \; \mathrm{TF\text{-}X]^-} \qquad (8)$$

$$\mathrm{PF} \; \cancel{\xrightleftharpoons[X\, =\, Cl^-,\, Br^-,\, PF_6^-]{BuN^+X^-}} \; \mathrm{PF\text{-}X]^-} \qquad (9)$$

The ESI mass spectrum of an equimolar mixture of the DF, TBACl, TBABr, TBAI, TBAF, on the other hand, showed exclusively the molecular ion peak for the DF-F anion complex (Figure 4.26). These results imply the extremely weak binding affinities of chloride, bromide, iodide, and hexafluoroposphate anions to the boroxines.

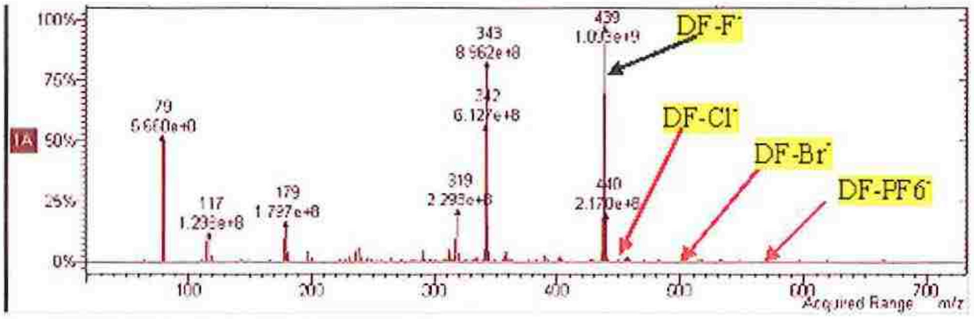

Figure 4.26. ESI/MS spectrum of an equimolar mixture of DF , TBACl, TBABr, TBAI, TBAF.

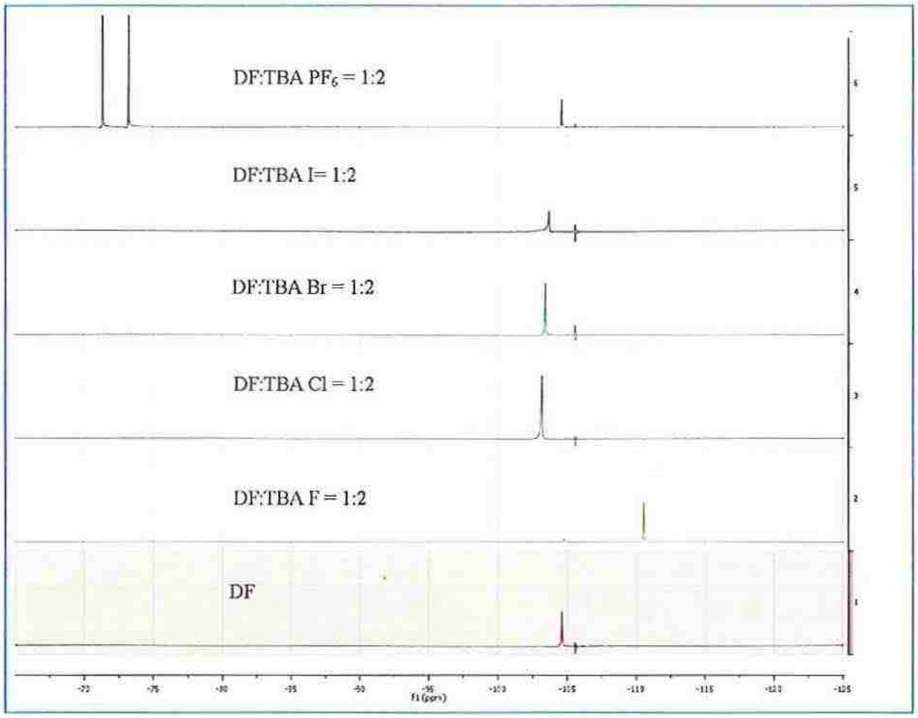

Figure 4.27. ^{19}F (376 MHz) NMR spectra of DF in dichloromethane in the presence of 2 equivalents of tetrabutyl ammonium salts of anions , TBAF, TBACl, TBABr, TBAI, and $TBAPF_6$.

Our electrospray mass spectroscopic studies in combination with *ab intio* DFT theory show that the fluorinated boroxines are highly selective to fluoride anion binding, and their relative binding to other halide anions and hexafluorophosphate is insignificant. Using tandem ESI mass spectroscopy we have characterized the fragmentation patterns for the fluorinated boroxin-fluoride anion complexes and identified the first 1,3.sigmatropic shift of fluorine to boron. The activation barriers for the 1,3.fluoride anion migration to boron has been estimated as 32.3 kcal/mol at B3LYP/6-311G**.